Surveys in Geophysics
https://doi.org/10.1007/s10712-023-09780-1

Surface-Wave Anelasticity in Porous Media: Effects of Wave-Induced Mesoscopic Flow

Enjiang Wang[1,2] · Jiaxuan Yan[1] · Bingshou He[1,2] · Zhihui Zou[1,2] · José M. Carcione[3,4] · Jing Ba[3]

Received: 25 November 2022 / Accepted: 23 February 2023

Abstract
We study the anelastic properties (attenuation and velocity dispersion) of surface waves at an interface between a finite water layer and a porous medium described by Biot theory including the frequency-dependent effects due to mesoscopic flow. A closed-form dispersion equation is derived, based on potential functions and open and sealed boundary conditions (BC) at the interface. The analysis indicates the existence of high-order surface modes for both BCs and a slow true surface mode only for sealed BC. The formulation reduces to two particular cases in the absence of water and with infinite-thickness water layer, with the presence of pseudo-versions of Rayleigh and Stoneley waves. The mesoscopic flow affects the propagation of all the pseudo-surface waves, causing significant velocity dispersion and attenuation, whereas the effect of the BC is mainly evident at high frequencies, due to the presence of the slow Biot wave. The mesoscopic-flow peak moves to low frequencies as the thickness of the water layer increases. In all cases, the true surface wave resembles the slow P2 wave, and is hardly affected by the flow.

Keywords Surface waves · Velocity dispersion · Attenuation · Mesoscopic flow · Biot theory · Boundary conditions

Article Highlights

- We study the velocity dispersion and attenuation of surface waves at an interface between a water layer and a porous medium described by an effective Biot theory, where the mesoscopic flow plays an important role
- We also consider the cases where the thickness of the water layer is zero and infinity

✉ Jing Ba
jba@hhu.edu.cn

[1] Key Lab of Submarine Geosciences and Prospecting Techniques, MOE, College of Marine Geosciences, Ocean University of China, Qingdao 266100, China

[2] Frontiers Science Center for Deep Ocean Multispheres and Earth System, Qingdao 266100, China

[3] School of Earth Sciences and Engineering, Hohai University, Nanjing 211100, China

[4] National Institute of Oceanography and Applied Geophysics - OGS, Trieste, Italy

- The examples reveal the nature of the surface waves and how the mesoscopic flow affects their propagation

1 Introduction

The propagation of surface waves is of interest in many fields, including geotechnical engineering, seismology, borehole logging and exploration geophysics (Markov 2009; Norris 1989; Pan et al. 2019; Tang and Cheng 1996; Xia et al. 2012). A detailed investigation in porous media has potential in revealing medium properties, such as permeability, porosity and saturation, which are important for reservoir characterization and fluid detection. For instance, Stoneley waves have been successfully used to estimate the formation permeability (Tang and Cheng 1996; Zhang and Müller 2019).

A phenomenological description of wave propagation in porous media was initiated by Biot (1956, 1962). He considered the media as a frame (matrix or skeleton), fully saturated with a single fluid, and established the constitutive (stress–strain) relations. In addition to the classical fast compressional and shear waves, the theory predicts a new slow compressional mode, which is diffusive at low frequencies and wave-like at high frequencies. The superposition of all these waves at an interface generates surface modes, whose features are different from those of the non-porous case. Basically, the surface modes become dissipative and dispersive due to losses by mode conversion to the slow wave (Deresiewicz 1962; Zhang et al. 2011). Considering a free surface of a porous medium, Deresiewicz (1962) confirmed the existence of a Rayleigh wave and analyzed its anelastic characteristics. Tajuddin (1984) examined the effects of permeable and impermeable boundaries on the Rayleigh waves. Partially permeable boundaries were investigated by Zhang et al. (2011), predicting a second surface wave, which closely resembles the bulk slow P2 wave, but appearing only at impermeable and partially permeable interfaces.

Surface waves at a liquid-porous medium interface were also studied (Chao et al. 2006; Feng and Johnson 1983a; Gubaidullin et al. 2004). Deresiewicz (1964) considered Stoneley waves in a Biot half-space with open-pore boundary conditions (BC), where he derived asymptotic expressions at low frequencies. Feng and Johnson (1983a) predicted a true surface wave and pseudo-Rayleigh and Stoneley waves (e.g., Carcione 2022). The true surface waves travel slower than all the body waves, and mainly appear under sealed-pore boundaries. The pseudo-Stoneley wave travels with a velocity between the bulk fluid sound speed and those of the slow modes, whereas the pseudo-Rayleigh wave propagates slower than the P1 (fast) and SV waves. These two waves leak part of their energies into slower mode as they propagate along the interface, and therefore are called pseudo-surface waves. If the liquid density tends to zero, the pseudo-Rayleigh wave becomes the classical Rayleigh one. Most predictions were validated experimentally by sonic measurements (Adler and Nagy 1994; Mayes et al. 1986), numerically by algorithms based on a domain-decomposition approach (Sidler et al. 2010) and analytically by a Green function using the Cagniard-de Hoop technique (Feng and Johnson 1983b). Gubaidullin et al. (2004) considered the viscous interaction between the fluid and solid and investigated numerically the frequency dependence of the velocities and damping coefficients of the three surface modes. Using an inverse Fourier transform, Han et al. (2017) obtained time-domain waveforms of the surface waves at a fluid-porous medium interface. Other studies regard propagation at an interface between two fluid-saturated porous media (Markov 2009) and between a liquid and layered porous media (Qiu et al. 2019).

However, Biot theory considers a macroscopic flow and cannot describe the broadband dispersion and attenuation of in situ rocks. Realistic attenuation is induced by fluid flow at various scales, including the microscopic and mesoscopic ones (Carcione et al. 2010; Carcione 2022; Müller et al. 2010). The squirt-flow model considers the microscopic scale (Carcione and Gurevich 2011; Dvorkin and Nur 1993; Dvorkin et al. 1995). It typically occurs at ultrasonic frequencies with fluid flowing from compliant regions (cracks, grain contacts) to the stiffer ones (pores). Using this model, Sharma (2018) investigated the properties of Rayleigh waves, predicting an additional (second) Rayleigh wave, which travels faster. On the other hand, the mesoscopic-flow mechanism accounts for attenuation at seismic frequencies (e.g., Carcione et al. 2010; Carcione 2022; Masson and Pride 2007; Müller et al. 2010; Pride et al. 2004; Zhao et al. 2015; Zhang et al. 2021). It occurs due to the heterogeneities much larger than the pore size but smaller than the wavelength. This mechanism appears in double-porosity theories. Pride and Berryman (2003a, 2003b) considered a composite of two isotropic porous materials (or phases) and developed a double-porosity model by applying a volume averaging based on Biot theory. A complex frequency-dependent compressibility law is introduced to describe the fluid transfer between the porous constituents. The double-porosity model reduces to an effective Biot theory involving complex and frequency-dependent moduli (Pride et al. 2004). It provides the basis for developing an upscaled poroviscoelastic formulation for seismic wave modeling in real media (Liu et al. 2009, 2018). The model has been applied by Liu et al. (2016) to analyze the velocity dispersion of borehole guided waves. On the other hand, Ba et al. (2011) developed a double-porosity model based on the Biot theory of poroelasticity and the Rayleigh model of bubble oscillations. The mesoscopic flow is described by a generalization of Rayleigh theory of liquid collapse of a spherical cavity. This model was applied by Sharma (2014) to study the propagation of Rayleigh waves. In addition, patchy-saturation models have also been developed to explain the wave loss (Chao et al. 2006; Lo et al. 2005; Lo 2008; Masson and Pride 2011; Sharma 2012; Wang et al. 2022; Zhao et al. 2017, 2021; Zhang et al. 2014, 2022).

Fluid flow affects the propagation of body waves and hence the surface waves (Dahl and Spikes 2017; Sharma 2014). The effect of macroscopic flow on the propagations of surface modes, including the Rayleigh and Stoneley waves, has been extensively studied by using the Biot theory (e.g., Deresiewicz 1962, 1964; Feng and Johnson 1983a; Gubaidullin et al. 2004; Markov 2009; Tajuddin 1984; Zhang et al. 2011). Basically, mode conversion into slow waves causes the Rayleigh and Stoneley waves to be pseudo-modes. Moreover, the frequency-dependent propagation can be significantly affected by the BC (Feng and Johnson 1983a; Tajuddin 1984; Zhang et al. 2011). Specifically, sealed or partially permeable BCs can induce an additional slow true surface mode, which closely resembles the slow P2 wave (Zhang et al. 2011), a mode that has been experimentally observed by Adler and Nagy (1994). Because only the macroscopic flow is considered, those results are mostly applicable at high frequencies. To study the broadband surface-wave propagation, the microscopic- and mesoscopic-flow mechanisms have been considered. The related theories include the squirt-flow model (Dahl and Spikes 2017; Sharma 2018), the patchy-saturation model (Chao et al. 2006; Lo 2008; Sharma 2012; Zhang et al. 2014), and the double-porosity model (Dai et al. 2006; Sharma 2014). In particular, Dahl and Spikes (2017) analyzed the effects of squirt flow on borehole acoustic wave modes based on the Chapman model, where the Stoneley wave can be significantly affected. Chao et al. (2006) investigated the properties of pseudo-Rayleigh and pseudo-Stoneley waves that propagate between a fluid and a partially saturated medium. The theory is based on a modified Biot model that takes into account the interaction among the gas bubbles, liquid and solid phases of the medium. Rayleigh-wave propagation at the surface of a

partially saturated medium was investigated by Sharma (2012). The results imply the significant dependence of the surface-wave dispersion and attenuation on saturation. Moreover, surface-wave dispersion in the presence of double-porosity heterogeneities has been considered, where the studies mainly focus on Rayleigh waves. Specifically, using the model of Ba et al. (2011), Sharma (2014) studied the Rayleigh wave propagation. The presence of mesoscopic flow enhances the dispersive behavior of these waves. The same problem was analyzed by Dai et al. (2006) using the theory of Pride and Berryman (2003a, 2003b), without the mesoscopic-flow effect. The effects of double-porosity mesoscopic flow on the propagation of various surface waves, particularly Stoneley modes, have not been fully analyzed. Such an analysis is of interest in exploration geophysics and borehole logging.

The aim of the present work is to explore the effect of double-porosity mesoscopic flow on the broadband propagation of various surface modes, including the pseudo-waves. We obtain the solutions for a flat interface separating a water layer and an effective Biot half-space, depending on the liquid thickness and medium properties. We choose the effective Biot model rather than the double-porosity theory for two reasons. First, it describes the mesoscopic-flow attenuation simply by using complex and frequency-dependent coefficients (Pride et al. 2004). Second, the equations have the same form as the classical Biot theory and hence the results are comparable to the results of Feng and Johnson (1983a), Gubaidullin et al. (2004) and Zhang et al. (2011). The paper proceeds as follows. We first briefly review the effective Biot theory and present its plane-wave solution. Then, we derive closed-form dispersion equations for the surface-wave propagation, based on potentials and suitable BC. Next, examples are presented to analyze the dispersion and attenuation of the related surface waves, including the pseudo-Rayleigh and Stoneley modes.

2 Effective Biot Theory

In the double-porosity model (Pride et al. 2004), the heterogeneous rock is described as a composite of two porous phases, namely the host phase (1) and the inclusion phase (2), having different hydraulic and elastic properties, but saturated by a single fluid. When phase 2 is totally embedded in the host phase, the double-porosity theory reduces to an effective single-porosity Biot model. The effect of mesoscopic flow is described by the complex stiffness moduli.

Defining the displacement vectors of the matrix and fluid relative to the solid as $\mathbf{u}$ and $\mathbf{w}$, respectively, and using a time dependence of $\exp(-\mathrm{i}\omega t)$, where ω is the angular frequency, the generalized compressibility laws (constitutive equations) are

$$\begin{bmatrix} \nabla \cdot \mathbf{v} \\ \nabla \cdot \mathbf{q} \end{bmatrix} = \mathrm{i}\omega \begin{bmatrix} a_{11}^* & a_{12}^* \\ a_{12}^* & a_{22}^* \end{bmatrix} \begin{bmatrix} p_\mathrm{c} \\ p_\mathrm{f} \end{bmatrix}, \tag{1}$$

$$-\mathrm{i}\omega \boldsymbol{\sigma}^D = \mu(\omega)[\nabla \mathbf{v} + (\nabla \mathbf{v})^\mathrm{T} - \frac{2}{3}\nabla \cdot \mathbf{v}\mathbf{I}], \tag{2}$$

where $\mathbf{v} = -\mathrm{i}\omega\mathbf{u}$ is the average particle velocity of the solid, $\mathbf{q} = -\mathrm{i}\omega\mathbf{w}$ is the macroscopic fluid flux, $\mathbf{I}$ is the second-order identity matrix, $\mu(\omega)$ is the complex and frequency-dependent shear modulus, $\boldsymbol{\sigma}^D$ is the average deviatoric stress tensor, p_c is the total average confining pressure acting on the averaging volume of the composite, and p_f is the average fluid pressure. The coefficients a_{ij}^* are given in Appendix A.

Introducing the total stress $\sigma_{ij} = \sigma_{ij}^D - p_\mathrm{c}\delta_{ij}$, where δ_{ij} is the Kronecker delta, and the relation

$$\begin{bmatrix} K^{\text{sat}} & \alpha M \\ \alpha M & M \end{bmatrix} = \begin{bmatrix} a_{11}^* & a_{12}^* \\ a_{12}^* & a_{22}^* \end{bmatrix}^{-1} = \frac{1}{a_{11}^* a_{22}^* - (a_{12}^*)^2} \begin{bmatrix} a_{22}^* & -a_{12}^* \\ -a_{12}^* & a_{11}^* \end{bmatrix}, \tag{3}$$

and using Eqs. (1) and (2), we have

$$\begin{aligned} \sigma_{ij} =& (\lambda_{\text{c}} u_{i,i} + \alpha M w_{i,i})\delta_{ij} + \mu(u_{i,j} + u_{j,i}), \\ p_{\text{f}} =& -\alpha M u_{i,i} - M w_{i,i}, \end{aligned} \tag{4}$$

with $\lambda_{\text{c}} = K^{\text{sat}} - \frac{2}{3}\mu$, and the comma preceding an index indicates spatial differentiation. Equation (4) is the same as the classical Biot theory (1962), except for that the quantities K^{sat}, α and M are frequency-dependent, which can be expressed in terms of the effective drained bulk modulus $K_D(\omega)$ and effective Skempton coefficient $B(\omega)$ as

$$\frac{1}{K^{\text{sat}}} = \frac{1}{K_D(\omega)} + B(\omega) a_{12}^*(\omega), \quad \alpha = \frac{1 - K_D(\omega)/K^{\text{sat}}}{B(\omega)}, \quad M = K^{\text{sat}} \frac{B(\omega)}{\alpha}, \tag{5}$$

where

$$\frac{1}{K_D(\omega)} = a_{11}^*(\omega), \qquad B(\omega) = -\frac{a_{12}^*(\omega)}{a_{22}^*(\omega)}, \tag{6}$$

which are the same as those of Pride et al. (2004). In the presence of fluid pressure differences between the two phases, fluid pressure equilibration results into frequency-dependent K_D and B.

The conservation of momentum is

$$\nabla \cdot \boldsymbol{\sigma}^D - \nabla p_{\text{c}} = -\text{i}\omega(\rho \mathbf{v} + \rho_{\text{f}} \mathbf{q}), \tag{7}$$

where $\rho = \phi\rho_{\text{f}} + (1 - \phi)\rho_{\text{s}}$ is the density of the composite, with ϕ being the total porosity (see Appendix A), and ρ_{f} and ρ_{s} the densities of the fluid and solid grain, respectively.

The effective Darcy law, allowing for fluid coupling the two phases, is

$$\mathbf{q} = -\frac{\kappa(\omega)}{\eta}(\nabla p_{\text{f}} - \text{i}\omega\rho_{\text{f}} \mathbf{v}), \tag{8}$$

where $\kappa(\omega)$ is the effective dynamic permeability of the composite, which can be obtained by taking the harmonic mean of the constituents as (Pride et al. 2004)

$$\frac{1}{\kappa(\omega)} = \frac{v_1}{\kappa_1(\omega)} + \frac{v_2}{\kappa_2(\omega)}, \tag{9}$$

where $\kappa_i(\omega)$ is the dynamic permeability of porous phase i, given by (Johnson et al. 1987),

$$\kappa_i(\omega) = \frac{\kappa_i}{\left[1 - \frac{\text{i}}{2}\tau_i \kappa_i \rho_{\text{f}} \omega/(\eta\phi_i)\right]^{1/2} - \text{i}\tau_i \kappa_i \rho_{\text{f}} \omega/(\eta\phi_i)}, \quad i = 1, 2, \tag{10}$$

where τ_i is the tortuosity of phase i.

Note that equation (8) considers no fluid–solid inertial coupling, and consequently differs from the classical Biot theory. To take the inertial coupling into account, we generalize this equation as

$$\mathbf{q} = -\frac{\kappa(\omega)}{\eta}(\nabla p_{\mathrm{f}} - \mathrm{i}\omega\rho_{\mathrm{f}}\mathbf{v} - \mathrm{i}\omega m\mathbf{q}), \tag{11}$$

where $m = \tau\rho_{\mathrm{f}}/\phi$, with an effective tortuosity $\tau = 0.5 + 0.5/\phi$ is considered for spherical grains (Berryman and Wang 2000).

3 Plane-wave Solution

In the uniform (homogeneous) case, the averaged displacement vectors of the matrix $\mathbf{u}$ and fluid $\mathbf{U}(= \mathbf{w}/\phi + \mathbf{u})$, the fluid stress $\sigma = -\phi p_{\mathrm{f}}$ and solid stress components $\tau_{ij} = \sigma_{ij} - \sigma\delta_{ij}$ can be used, and equation (4) becomes

$$\begin{aligned} \tau_{ij} =& \big(Au_{i,i} + QU_{i,i}\big)\delta_{ij} + N(u_{i,j} + u_{j,i}), \\ \sigma =& Qu_{i,i} + RU_{i,i}, \end{aligned} \tag{12}$$

where

$$R = M\phi^2, \quad Q = \alpha M\phi - M\phi^2, \quad N = \mu, \quad A = \lambda_{\mathrm{c}} - 2Q - R. \tag{13}$$

The equations of momentum conservation become

$$\begin{aligned} \tau_{ij,j} =& \rho_{11}\ddot{u}_i + \rho_{12}\ddot{U}_i + b(\dot{u}_i - \dot{U}_i), \\ \sigma_{,i} =& \rho_{12}\ddot{u}_i + \rho_{22}\ddot{U}_i - b(\dot{u}_i - \dot{U}_i), \end{aligned} \tag{14}$$

where

$$\begin{aligned} \rho_{12} =& \phi\rho_{\mathrm{f}} - m\phi^2, \quad \rho_{22} = m\phi^2, \quad b = \phi^2\eta/\kappa, \\ \rho_{11} =& \rho - 2\rho_{\mathrm{f}}\phi + m\phi^2. \end{aligned} \tag{15}$$

Based on equations (12) and (14), we obtain the effective Biot equations in terms of $\mathbf{u}$ and $\mathbf{U}$ as

$$\begin{aligned} N\nabla^2\mathbf{u} + (A+N)\nabla(\nabla\cdot\mathbf{u}) + Q\nabla(\nabla\cdot\mathbf{U}) =& \rho_{11}\ddot{\mathbf{u}} + \rho_{12}\ddot{\mathbf{U}} + b(\dot{\mathbf{u}} - \dot{\mathbf{U}}), \\ Q\nabla(\nabla\cdot\mathbf{u}) + R\nabla(\nabla\cdot\mathbf{U}) =& \rho_{12}\ddot{\mathbf{u}} + \rho_{22}\ddot{\mathbf{U}} - b(\dot{\mathbf{u}} - \dot{\mathbf{U}}), \end{aligned} \tag{16}$$

which have the same form as the classical Biot theory (Biot 1962) with A, N, Q and R frequency-dependent.

A plane-wave analysis of Eq. (16) predicts three wave modes, namely, the fast P1 wave, the slow P2 wave and the shear wave. Following Feng and Johnson (1983a), the complex velocities of the two P waves are

$$V_{\pm}^2 = \frac{\Delta \pm \sqrt{\Delta^2 - 4(\tilde{\rho}_{11}\tilde{\rho}_{22} - \tilde{\rho}_{12}^2)(PR - Q^2)}}{2(\tilde{\rho}_{11}\tilde{\rho}_{22} - \tilde{\rho}_{12}^2)}, \mathbf{U}_{\pm} = -G_{\pm}\mathbf{u}_{\pm}, \tag{17}$$

where $P = A + 2N$,

$$\tilde{\rho}_{11} = \rho_{11} + \mathrm{i}b/\omega, \quad \tilde{\rho}_{12} = \rho_{12} - \mathrm{i}b/\omega, \quad \tilde{\rho}_{22} = \rho_{22} + \mathrm{i}b/\omega,$$
$$\Delta \equiv P\tilde{\rho}_{22} + R\tilde{\rho}_{11} - 2Q\tilde{\rho}_{12}, G_{\pm} = \frac{V_{\pm}^2\tilde{\rho}_{11} - P}{V_{\pm}^2\tilde{\rho}_{12} - Q}, \tag{18}$$

where V_+ and V_- denote the velocities of the fast P1 and slow P2 waves, and $-G_+$ and $-G_-$ denote the corresponding amplitude ratios between the average displacements of the fluid $\mathbf{U}$ and that of the solid $\mathbf{u}$, respectively.

The velocity of the shear wave is (Feng and Johnson 1983a)

$$V_{\mathrm{sh}}^2 = \frac{N}{(1-\phi)\rho_{\mathrm{s}} + (1 - 1/\tilde{\tau})\phi\rho_{\mathrm{f}}}, \quad \mathbf{U}_{\mathrm{sh}} = \frac{\tilde{\tau} - 1}{\tilde{\tau}}\mathbf{u}_{\mathrm{sh}}, \tag{19}$$

where $\tilde{\tau} = \tau + \mathrm{i}b/(\omega\phi\rho_{\mathrm{f}})$, and $\dfrac{\tilde{\tau} - 1}{\tilde{\tau}}$ represents the amplitude ratio.

Using the complex velocities, the corresponding phase velocity and dissipation factor are (Carcione 2022)

$$V_{pi} = \left[\mathrm{Re}\left(\frac{1}{V_i}\right)\right]^{-1}, \quad Q_i^{-1} = -\frac{\mathrm{Im}(V_i^2)}{\mathrm{Re}(V_i^2)}, \quad i = +, -, \mathrm{sh}, \tag{20}$$

where, "Re" and "Im" represent real and imaginary parts and indexes '+', '−' and 'sh' correspond to the fast P1, slow P2 and SV waves, respectively, which will be denoted as 1, 2 and 3 in the following. The negative sign in equation (20) for the definition of dissipation factor is due to the fact that we use the Fourier convention $\exp(-\mathrm{i}\omega t)$.

4 Surface-Wave Propagation

We consider a water layer of thickness H (denoted as medium I) overlying an effective Biot half-space (denoted as medium II), as shown in Fig. 1. The z-axis is perpendicular to the interface in the direction of increasing depth into the effective Biot medium. The interface is located at $z = 0$, and hence $-H < z < 0$ defines the water layer, whereas $z > 0$ represents the porous half-space.

The equation of motion of the fluid is

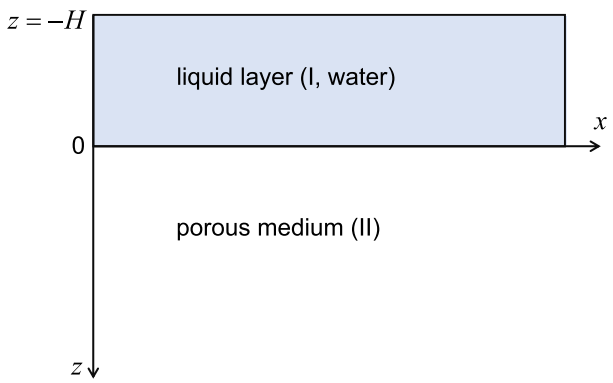

Fig. 1 Geometrical model

$$\frac{\partial^2 \boldsymbol{\Phi}_0}{\partial x^2} + \frac{\partial^2 \boldsymbol{\Phi}_0}{\partial z^2} = \frac{1}{v_0^2}\frac{\partial^2 \boldsymbol{\Phi}_0}{\partial t^2}, \tag{21}$$

where $\boldsymbol{\Phi}_0$ is the potential, $v_0 = (\lambda_0/\rho_0)^{1/2}$ is the velocity, with λ_0 and ρ_0 being the bulk modulus and density, respectively.

The general solution of Eq. (21) for surface-wave propagation is

$$\boldsymbol{\Phi}_0 = \left[D_0 \exp(kz\xi_0) + E_0 \exp(-kz\xi_0)\right] \exp[\mathrm{i}(kx - \omega t)], \tag{22}$$

where D_0 and E_0 are the amplitudes, k is the horizontal wavenumber and $\xi_0 = (1 - c^2/v_0^2)^{1/2}$, with $c = \omega/k$ being the surface-wave velocity.

The displacements and stresses corresponding to Eq. (21) are

$$\mathbf{u}_0 = (u_x, u_z)^{\mathrm{T}} = \nabla \boldsymbol{\Phi}_0, \quad \tau_{xz} = 0, \quad -p_{\mathrm{f}} = \lambda_0 \left(\frac{\partial^2 \boldsymbol{\Phi}_0}{\partial x^2} + \frac{\partial^2 \boldsymbol{\Phi}_0}{\partial z^2} \right). \tag{23}$$

On the other hand, the displacements of the solid and fluid of the effective Biot medium are

$$\begin{aligned} u_x &= \frac{\partial \boldsymbol{\Phi}_1}{\partial x} + \frac{\partial \boldsymbol{\Phi}_2}{\partial x} - \frac{\partial \boldsymbol{\Phi}_3}{\partial z}, \quad u_z = \frac{\partial \boldsymbol{\Phi}_1}{\partial z} + \frac{\partial \boldsymbol{\Phi}_2}{\partial z} + \frac{\partial \boldsymbol{\Phi}_3}{\partial x}, \\ U_x &= \nu_1 \frac{\partial \boldsymbol{\Phi}_1}{\partial x} + \nu_2 \frac{\partial \boldsymbol{\Phi}_2}{\partial x} - \nu_3 \frac{\partial \boldsymbol{\Phi}_3}{\partial z}, \quad U_z = \nu_1 \frac{\partial \boldsymbol{\Phi}_1}{\partial z} + \nu_2 \frac{\partial \boldsymbol{\Phi}_2}{\partial z} + \nu_3 \frac{\partial \boldsymbol{\Phi}_3}{\partial x}, \end{aligned} \tag{24}$$

where $\boldsymbol{\Phi}_j (j = 1, 2, 3)$ are the potentials associated to the fast P1, slow P2 and SV waves, and $\nu_1 = -G_+$, $\nu_2 = -G_-$, and $\nu_3 = \dfrac{\tilde{\tau} - 1}{\tilde{\tau}}$ are the amplitude ratios. For harmonic propagation, the potentials are

$$\boldsymbol{\Phi}_j = D_j \exp[\mathrm{i}(kx - \omega t) - kz\xi_j], \quad \xi_j = \sqrt{1 - c^2/V_j^2}, \quad j = 1, 2, 3, \tag{25}$$

where D_j are the amplitudes, $V_1 = V_+$, $V_2 = V_-$ and $V_3 = V_{\mathrm{sh}}$ are the complex velocities of the fast P1, slow P2 and SV waves. Using Eqs. (24) and (25), the total stress σ_{ij} and pore-fluid pressure p_{f} can be obtained using Eq. (4).

4.1 Boundary Conditions

At the free surface of the liquid $z = -H$, we have

$$(p_{\mathrm{f}})_{\mathrm{I}} = 0. \tag{26}$$

Then, we obtain

$$E_0 = -D_0 \exp(-2kH\xi_0), \tag{27}$$

and hence equation (22) is simplified as

$$\boldsymbol{\Phi}_0 = D_0 \exp(-kH\xi_0) \Big\{ \exp[k\xi_0(z + H)] - \exp[-k\xi_0(z + H)] \Big\} \exp[\mathrm{i}(kx - \omega t)]. \tag{28}$$

At the interface ($z = 0$), the following BC are given (Deresiewicz and Skalak 1963)

$$
\begin{aligned}
&(\sigma_{xz})_{\mathrm{II}} = 0,\\
&(-p_{\mathrm{f}})_{\mathrm{I}} = (\sigma_{zz})_{\mathrm{II}},\\
&(u_z)_{\mathrm{I}} = (u_z)_{\mathrm{II}} + (w_z)_{\mathrm{II}},\\
&(p_{\mathrm{f}})_{\mathrm{I}} - (p_{\mathrm{f}})_{\mathrm{II}} = Z_I(\dot{w}_z)_{\mathrm{II}},
\end{aligned}
\tag{29}
$$

where the first two equations represent the continuity of the normal and shear stresses, the third one is the continuity of the vertical displacement, and Z_I is the so-called interface impedance (e.g., Carcione et al. 2021; Carcione 2022). In particular, $Z_I = 0$ and $Z_I = \infty$ are two special cases representing fully open and sealed BC, respectively (Qi et al. 2021). The former indicates a perfect hydraulic connection between the fluid and the porous medium, with free flow in the pores. This can occur, for instance, when free gas or water migrates from shallow sediments through open fractures into seawater. As a contrast, the latter implies the nonalignment of the pore space with the overlying liquid, which can be accomplished by an impermeable membrane at the interface. Basically, the BC are the requirements to ensure uniqueness of solution at the interface within the framework of the Biot theory (Deresiewicz and Skalak 1963), which are also adopted in previous works (e.g., Chao et al. 2006; Deresiewicz 1964; Feng and Johnson 1983a; Sharma 2018).

The above BC form a system of equations of order four for the unknown amplitudes $\mathbf{D} = [D_0, D_1, D_2, D_3]^{\mathrm{T}}$ as follows:

$$
\mathbf{MD} = \mathbf{0}, \tag{30}
$$

where the elements of $\mathbf{M}$ are given in Appendix B.

4.2 Special Cases

When $H = 0$, the problem given in Fig. 1 reduces to the propagation of Rayleigh waves at the free surface of an effective Biot half-space. The corresponding BC in equation (29) reduce to

$$
\begin{aligned}
(\sigma_{xz})_{\mathrm{II}} &= 0,\\
(\sigma_{zz})_{\mathrm{II}} &= 0,\\
-(p_{\mathrm{f}})_{\mathrm{II}} &= Z_I(\dot{w}_z)_{\mathrm{II}},
\end{aligned}
\tag{31}
$$

which forms a matrix equation of order three for the unknown amplitudes $\mathbf{D}^{(1)} = [D_1, D_2, D_3]^{\mathrm{T}}$ as

$$
\mathbf{M}^{(1)}\mathbf{D}^{(1)} = \mathbf{0}, \tag{32}
$$

where the elements of $\mathbf{M}^{(1)}$ can be obtained by eliminating the first column and the third row of matrix $\mathbf{M}$ as

$$
\mathbf{M}^{(1)} = \begin{bmatrix} M_{01} & M_{02} & M_{03} \\ M_{11} & M_{12} & M_{13} \\ M_{31} & M_{32} & M_{33} \end{bmatrix}. \tag{33}
$$

Alternatively, if $H = +\infty$, the problem becomes the same as that of Feng and Johnson (1983a), corresponding to the propagation of Stoneley (Scholte) waves at the interface

between a liquid half-space and an effective Biot half-space. In this case, $E_0 = 0$, and the potential $\boldsymbol{\Phi}_0$ becomes

$$\boldsymbol{\Phi}_0 = D_0 \exp(kz\xi_0)\exp[\mathrm{i}(kx - \omega t)]. \tag{34}$$

At the interface, the BC in Eq. (29) remain the same, and the matrix equation becomes

$$\mathbf{M}^{(2)}\mathbf{D} = \mathbf{0}, \tag{35}$$

where the elements of $\mathbf{M}^{(2)}$ can be obtained from $\mathbf{M}$ by letting $H = +\infty$. Hence, the elements of the first column become

$$M_{00}^{(2)} = 0, \quad M_{10}^{(2)} = -\rho_0, \quad M_{20}^{(2)} = \xi_0, \quad M_{30}^{(2)} = -\rho_0, \tag{36}$$

whereas all the other elements of $\mathbf{M}^{(2)}$ are the same as those of $\mathbf{M}$.

In Appendix B, we show that the matrix equation (35) is identical to the one of Feng and Johnson (1983a), except that the elastic parameters used in (35) are frequency-dependent in the presence of mesoscopic-flow attenuation. Our equations better describe surface-wave propagation at lower frequencies, particularly at the exploration-geophysics band.

4.3 Dispersion Equation

A nontrivial solution of equation (30) requires that the determinant of matrix $\mathbf{M}$ must vanish, that is, $\det(\mathbf{M}) = 0$, which is the surface-wave dispersion equation. Because transcendental functions are involved, solving for the unknown complex velocity c is highly nonlinear. Here, we use the Muller iteration method (Muller 1956), to numerically obtain the solutions. The complex solutions imply that the surface waves are inhomogeneous, i.e., the propagation and attenuation directions do not coincide. Moreover, the waves should decay with increasing z in the porous half-space, indicating that any solution of c requires a positive real part for $k\xi_j = \dfrac{\omega}{c}\xi_j$ given in equation (25). The phase velocity and dissipation factor are

$$V = \left[\mathrm{Re}\left(\frac{1}{c}\right)\right]^{-1} \quad \text{and} \quad Q^{-1} = -\frac{\mathrm{Im}(c^2)}{\mathrm{Re}(c^2)}, \tag{37}$$

respectively.

Similarly,

$$\det(\mathbf{M}^{(1)}) = 0 \quad \text{and} \quad \det(\mathbf{M}^{(2)}) = 0 \tag{38}$$

are the dispersion relations corresponding to $H = 0$ and $H = +\infty$, respectively.

It has been shown that there are more than one surface mode (Feng and Johnson 1983a; Gubaidullin et al. 2004; Zhang et al. 2011). Using the classical Biot theory, Feng and Johnson (1983a) confirmed the existence of a "true" surface wave and pseudo-surface waves at the high-frequency range, depending on the BC and medium properties. Zhang et al. (2011) investigated the Rayleigh wave propagation at the free surface of Biot porous media and confirmed the existence of a second Rayleigh mode that propagates only for closed-pore and partially permeable conditions. All these surface modes can be affected by the mesoscopic flow.

4.4 Displacement Motions

Omitting $\exp[\mathrm{i}(kx-\omega t)]$, the displacements in the water layer I ($-H \le z < 0$) can be obtained from Eqs. (23) and (28) as

$$\begin{aligned}(u_x)^{\mathrm{I}} &= D_3 S_0 \mathrm{i}k\exp(-kH\xi_0)\Big\{\exp[k\xi_0(z+H)] - \exp[-k\xi_0(z+H)]\Big\},\\ (u_z)^{\mathrm{I}} &= D_3 S_0 k\xi_0\exp(-kH\xi_0)\Big\{\exp[k\xi_0(z+H)] + \exp[-k\xi_0(z+H)]\Big\},\end{aligned} \tag{39}$$

where $S_0 = D_0/D_3$ is the amplitude ratio.

Similarly, in the effective Biot medium II, defined by $z \ge 0$, the displacements are

$$\begin{aligned}(u_x)^{\mathrm{II}} &= (u_x + w_x)_{\mathrm{II}} = \frac{\partial \boldsymbol{\Phi}_1}{\partial x}c_1 + \frac{\partial \boldsymbol{\Phi}_2}{\partial x}c_2 - \frac{\partial \boldsymbol{\Phi}_3}{\partial z}c_3,\\ (u_z)^{\mathrm{II}} &= (u_z + w_z)_{\mathrm{II}} = \frac{\partial \boldsymbol{\Phi}_1}{\partial z}c_1 + \frac{\partial \boldsymbol{\Phi}_2}{\partial z}c_2 + \frac{\partial \boldsymbol{\Phi}_3}{\partial x}c_3,\end{aligned} \tag{40}$$

where $c_j = 1 - \phi + \phi v_j$, $j = 1, 2, 3$.

Substituting Eq. (25) into (40), we have

$$\begin{aligned}(u_x)^{\mathrm{II}} &= \sum_{j=1}^{2} \mathrm{i}kc_j D_3 S_j \exp(-kz\xi_j) + c_3 D_3 k\xi_3 \exp(-kz\xi_3),\\ (u_z)^{\mathrm{II}} &= -\sum_{j=1}^{2} k\xi_j c_j D_3 S_j \exp(-kz\xi_j) + c_3 D_3 \mathrm{i}k\exp(-kz\xi_3),\end{aligned} \tag{41}$$

with $S_j = D_j/D_3$, which can be determined from the singular system of BC (30) as

$$\begin{bmatrix} M_{00} & M_{01} & M_{02} \\ M_{10} & M_{11} & M_{12} \\ M_{20} & M_{21} & M_{22} \end{bmatrix} \begin{bmatrix} S_0 \\ S_1 \\ S_2 \end{bmatrix} = -\begin{bmatrix} M_{03} \\ M_{13} \\ M_{23} \end{bmatrix}, \tag{42}$$

for the case when $H \neq 0$, including $H = +\infty$. For $H = 0$, based on equation (32), the relation becomes

$$\begin{bmatrix} M_{01} & M_{02} \\ M_{11} & M_{12} \end{bmatrix} \begin{bmatrix} S_1 \\ S_2 \end{bmatrix} = -\begin{bmatrix} M_{03} \\ M_{13} \end{bmatrix}. \tag{43}$$

From the BC, the vertical displacements $(u_z)^{\mathrm{I}}$ and $(u_z)^{\mathrm{II}}$ at the interface $z = 0$ should be continuous, and their magnitudes decay significantly as the distance from the interface increases.

5 Examples

We consider the rock properties given in Table 1 (Pride and Berryman 2003a; Pride et al. 2004). We assume a concentric sphere geometry with inner radius $a = 1$ cm and outer radius $R = 3a$, so that the volume fractions are $v_2 = 0.037$ and $v_1 = 1 - v_2 = 0.963$. Correspondingly, the volume to internal surface ratio $V/S = R^3/(3a^2) = 9a$, and the characteristic length

Table 1 Properties of the porous medium

K_s (GPa)	μ_s (GPa)	ρ_s (kg/m^3)	ϕ_1	ϕ_2	κ_1 (darcy)	κ_2 (darcy)	a (cm)
38	44	2650	0.2	0.4	0.01	1	1

is determined by $L_1^2 = 99a^2/28$. The composite consists of sand grains with bulk modulus $K_s = 38$ GPa, shear modulus $\mu_s = 44$ GPa and density $\rho_s = 2650$ kg/m^3. Phase 2 represents small pockets where the grains are poorly bonded, with $\phi_2 = 0.4$ and $\kappa_2 = 1$ darcy. Phase 1 is a more consolidated shaly sandstone with $\phi_1 = 0.2$ and $\kappa_1 = 0.01$ darcy. The effective-medium relation $K_i^d = (1-\phi_i)K_s/(1+\tilde{c}_i\phi_i)$ is used to compute the drained bulk modulus K_i^d, where $\tilde{c}_i$ is the consolidation parameter. We consider $\tilde{c}_1 = 10$ and $\tilde{c}_2 = 200$ (Pride and Berryman 2003a). The dry-rock bulk modulus of the composite is computed as a harmonic average of the two constituent dry-rock moduli as $1/K^d = v_1/K_1^d + v_2/K_2^d$. The shear modulus μ of the composite is frequency independent in Pride and Berryman (2003a) and is given by $\mu = (1-\phi)\mu_s/(1+\tilde{c}_s\phi)$ with $\tilde{c}_s = 10$. Viscoelastic mechanisms, for example, the Cole-Cole theory, may be used to alternatively model the shear wave attenuation (Liu et al. 2018). The tortuosity of phase i is defined as $\tau_i = 0.5 + 0.5/\phi_i$ for spherical grains (Berryman and Wang 2000). The fluid saturating the porous medium is assumed to be the same as the overlying water and has the properties given in Table 2 (Gurevich et al. 2004).

Figures 2 and 3 show the phase velocities and dissipation factors of the three body waves as a function of frequency. The mesoscopic flow causes a significant P1-wave attenuation for frequencies smaller than 100 kHz, particularly at the exploration-geophysics band between 10 Hz and 1 kHz, and consequently induces a significant velocity dispersion of approximately 200 m/s, whereas it hardly affects the propagation of the slow P2 and SV modes. The reason is due to the fact that when a real-value shear modulus μ is used, the shear-wave velocity is independent on the mesoscopic-flow mechanism, as shown byEq. (19). The slow mode is dispersive at low frequencies and becomes wavelike at high frequencies. Even though its velocity is small, the propagation can remarkably influence the fast P1-wave energy and hence the properties of the surface wave, which carries information about the porous media. Basically, the presence of the slow P2 wave gives rise to a slow surface mode and transforms the Rayleigh and Stoneley waves into pseudo modes, which will be discussed in the following. At high frequencies, the effect of mesoscopic flow disappears and the Biot global flow plays a dominant role, causing another attenuation peak at around 1 MHz.

5.1 Surface Waves

We first consider $H = 0$ to study the propagation of Rayleigh-type waves at the free surface of a porous medium. Equation (38) gives two surface waves (denoted as R1 and R2), where R1 propagates faster than the slow P2 wave but slower than the shear wave, leaking part of its energy into the slow mode (pseudo-Rayleigh wave), whereas R2 propagates slower than the P2 wave and is a true surface (Stoneley) wave (Zhang et al. 2011).

Table 2 Fluid properties

	K_f (GPa)	η_f (Pa s)	ρ_f (kg/m^3)
Water	2.22	0.001	1000

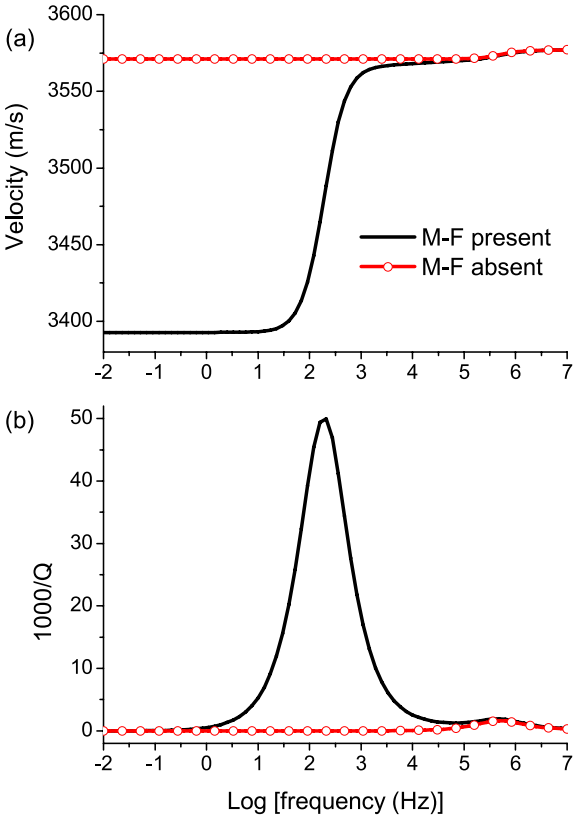

Fig. 2 Phase velocity (**a**) and dissipation factor (**b**) of the fast P1 wave as a function of frequency. The M-F refers to "mesoscopic-flow"

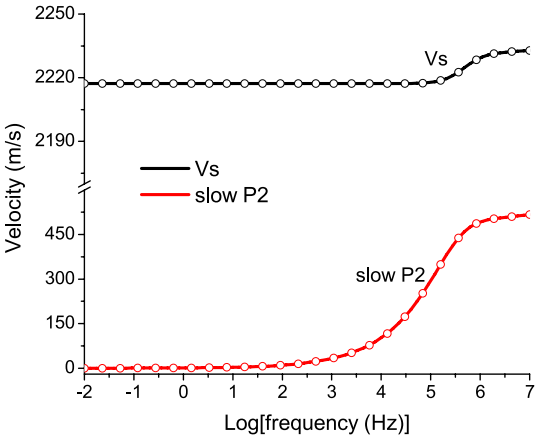

Fig. 3 Phase velocities of the slow P2 and shear waves as a function of frequency. The dotted and solid lines correspond to the results without and with the mesoscopic-flow attenuation, respectively

Figures 4 and 5 show the phase velocity and dissipation factor of the R1 wave as a function of frequency. We observe that the R1 wave propagates slower than the shear wave with a dimensionless velocity ratio of approximately 0.9, but it is more attenuated. The effect of the mesoscopic flow is mainly observed at frequencies less than 10

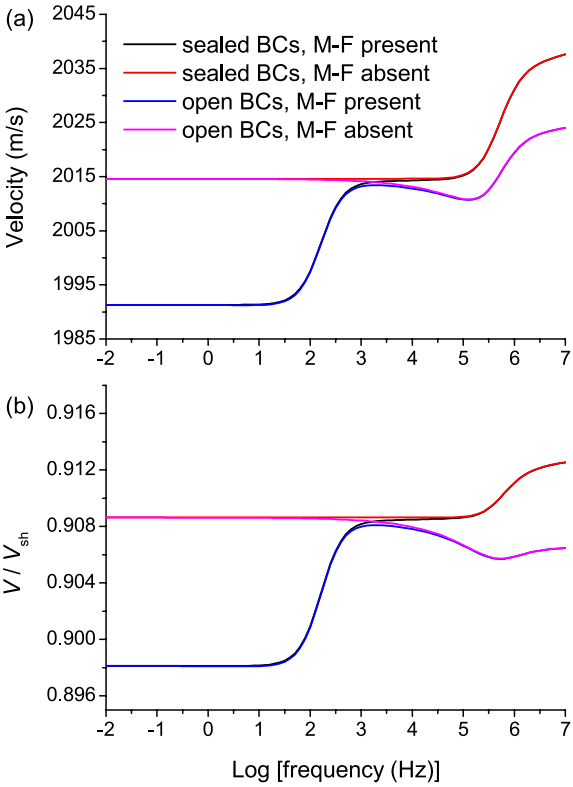

Fig. 4 Phase velocity (**a**) and phase dimensionless velocity (**b**) with respect to the shear wave of the pseudo-Rayleigh wave (R1) as a function of frequency, at the surface of a porous medium

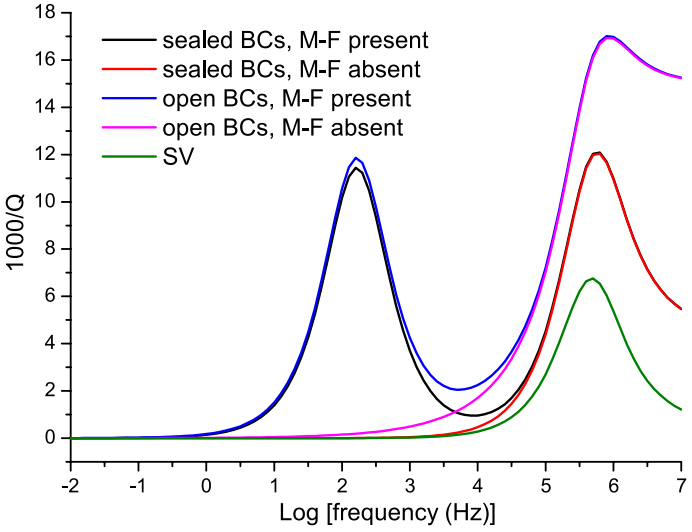

Fig. 5 Dissipation factor of the pseudo-Rayleigh wave (R1) at the surface of a porous medium. The result of the shear wave is plotted as a comparison

kHz, inducing an additional attenuation peak, particularly at the exploration-geophysics band between 10 Hz and 1 kHz, and consequently causing a quite significant velocity dispersion at low frequencies. The phenomenon is similar to the P1-wave propagation in Fig. 2. The second attenuation peak at high frequencies is due to the Biot global flow. The boundary conditions affect the propagation mainly at frequencies higher than 1 kHz. The reason is due to the fact that at low frequencies, the slow wave hardly propagates and the free surface becomes equivalent to the elastic (non-porous) one. The open-pore BC yield a lower velocity of R1 wave but imply a higher attenuation than the sealed-pore BC, possibly due to the energy transfer between the fast and slow wave modes through the open pores.

Figure 6 shows the phase velocity of the true surface mode R2. This mode is wave-like only at high frequencies for sealed-pore BC, and has a velocity slightly smaller than that of the slow P2 wave. At low frequencies, it becomes highly dispersive. Hence the presence of the slow surface mode is related to the impermeable BC. A similar true surface mode was observed by Zhang et al. (2011) using the classical Biot theory, where it is referred to as the true Stoneley wave. The influence of mesoscopic flow on R2 is negligible at all frequencies.

Figure 7 shows the absolute displacements of the R1 wave as a function of depth at a frequency of 100 Hz. The displacement decreases as the depth increases due to the energy decay and shows a critical depth of 40 m, approximately twice the R1 wavelength. The critical depth defined here refers to the depth at which the absolute displacements are approximately zero. The horizontal displacement shows a sharp variation at approximately 4 m, indicating a change in trajectory of the particle motions. In the presence of mesoscopic-flow attenuation, the displacement is more attenuated. At 100 Hz, the R2 wave hardly propagates and its displacements are not displayed.

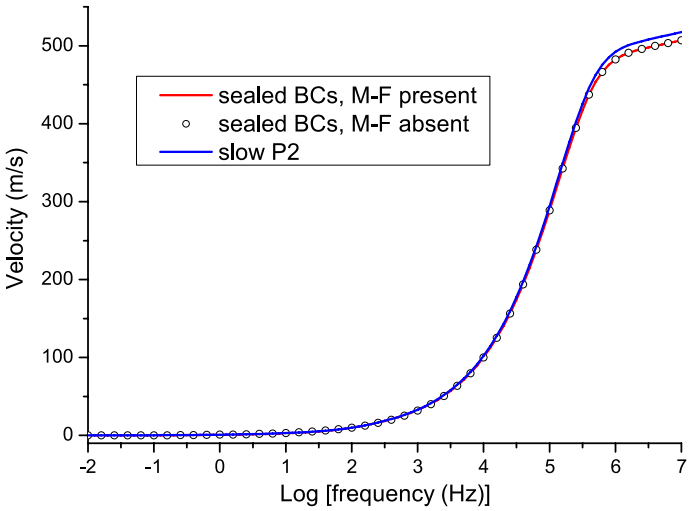

Fig. 6 Phase velocity of the true surface (Stoneley) wave (R2) at the surface of a porous medium. The phase velocity of the slow P2 wave is plotted in solid blue line as a comparison. The R2 wave does not propagate for the open-pore BC

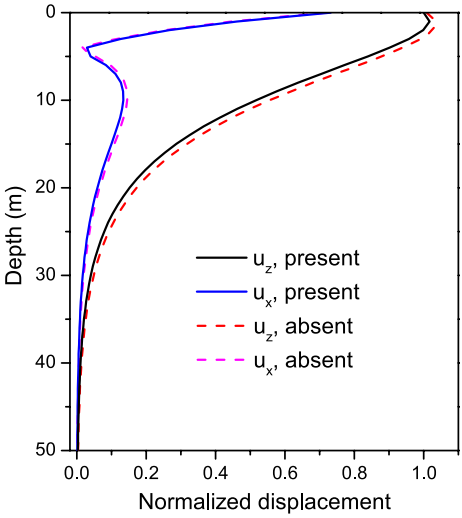

Fig. 7 Absolute values of the displacements of the R1 wave as a function of depth at 100 Hz. The displacements are normalized by the vertical u_z at the surface $z = 0$ when the mesoscopic-flow is present. The open-pore BC are used

5.2 Waves at a Liquid/Solid Interface

Next, we consider $H = +\infty$, the same problem studied by Feng and Johnson (1983a) using the classical Biot theory, to investigate the propagation of Stoneley and Rayleigh waves at the fluid/porous medium interface. Equation (38), with the constraint of $\mathrm{Re}(k\xi_j) > 0$, yields two surface waves. The first one propagates slower than the fluid bulk mode, but faster than the slow P2 wave, and hence it is called pseudo-Stoneley wave (Feng and Johnson 1983a). The second one propagates slower than all the body waves and leaks no energy, and is termed true Stoneley wave.

Figures 8 and 9 show the phase velocity and dissipation factor of the pseudo-Stoneley wave that exists for both sealed and open BC. We see that the mesoscopic flow mainly induces an attenuation peak at low frequencies, particularly at the exploration band around 100 Hz, and hence causes an observable velocity dispersion. Around 1 MHz, the Biot global flow results into another attenuation peak. The two peaks are weaker compared with those of the R1 wave in Fig. 5. The effect of the BC is mainly observed at frequencies higher than 1 kHz. Compared with the sealed-pore BC, the open one yields a stronger global-flow attenuation, and consequently a more significant dispersion, causing the velocity to be higher at high frequencies. The pseudo-Stoneley wave propagates slower than the acoustic wave in water, with a dimensionless velocity V/v_0 approximately equal to 0.97.

The true Stoneley wave exists only for sealed-pore BC, and its phase velocity is displayed in Fig. 10. Similar to the R2 wave, the true Stoneley wave resembles the bulk slow P2 wave, which is dispersive at low frequencies, and becomes wavelike at high frequencies with a slightly smaller velocity than the P2 wave. A similar wave at high frequencies was observed by Feng and Johnson (1983a), where they concluded that the true Stoneley mode is asymptotically the bulk slow wave. The effect of mesoscopic flow is negligible, similar to the P2 wave.

Figure 11 shows the absolute displacements of the pseudo-Stoneley wave at a frequency of 100 Hz. The vertical displacements are continuous at the interface, consistent with the BC, whereas the horizontal displacement in water is much larger. The displacements in water decay slower. The critical depths in the porous and water half-spaces are

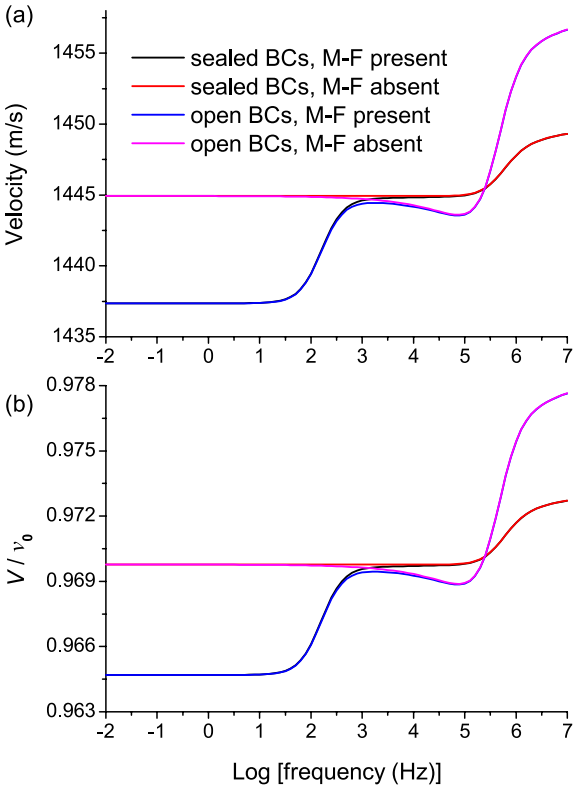

Fig. 8 Phase velocity (**a**) and phase dimensionless velocity with respect to v_0 (**b**) of the pseudo-Stoneley wave as a function of frequency, at the interface between water and a porous half-space

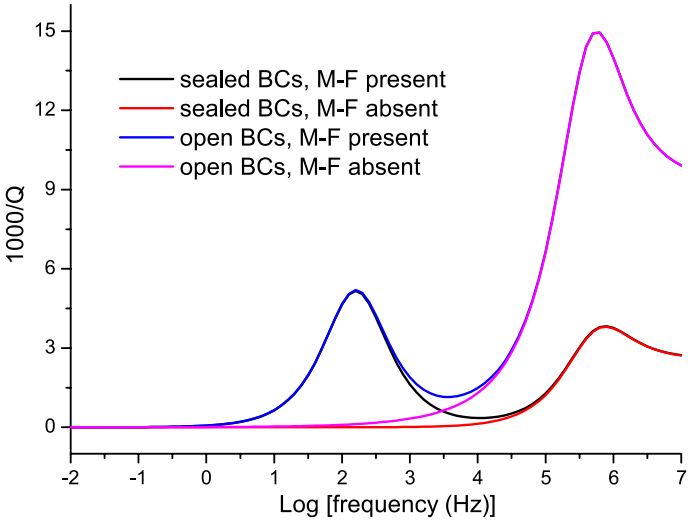

Fig. 9 Dissipation factor of the pseudo-Stoneley wave as a function of frequency, at the interface between water and a porous half-space

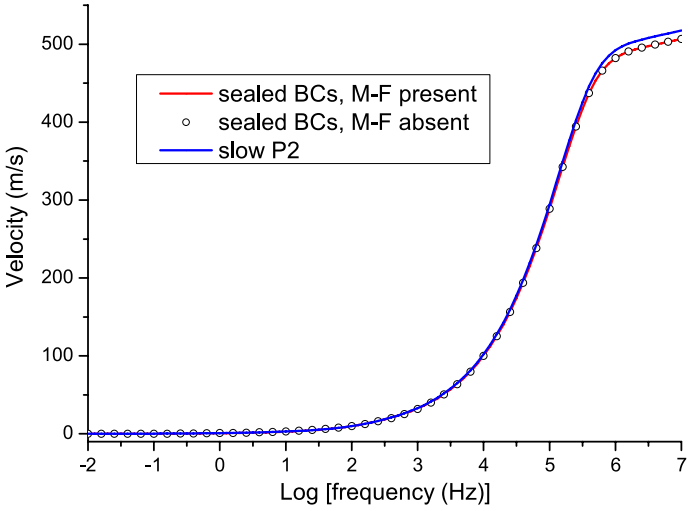

Fig. 10 Phase velocity of the true Stoneley wave at the interface between water and a porous half-space for sealed-pore BC. The result of the slow P2 wave is plotted in solid blue line as a comparison. The true Stoneley wave does not exist for the open-pore BC

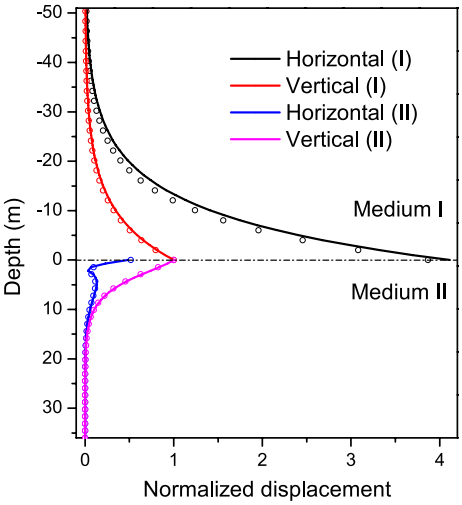

Fig. 11 Absolute values of the displacements of the pseudo-Stoneley wave as a function of depth at 100 Hz. The displacements are normalized by the vertical u_z at the surface $z = 0$ when the mesoscopic flow is present. The open-pore BC are used. The solid and dotted lines represent the results without and with mesoscopic-flow attenuation, respectively

approximately 15 m and 50 m, corresponding to 1 and 3.3 times the pseudo-Stoneley wavelength, respectively. The mesoscopic-flow attenuation slightly affects the displacements, and the effect is particularly significant for the horizontal displacement in water. Similar to the R1 wave in Fig. 7, a sharp variation of the absolute horizontal displacement in the porous half-space is observed.

All the above results are obtained with the restriction $\mathrm{Re}(k\xi_j) > 0$, a condition for energy decay of surface waves away from the interface, which is also required by Feng and Johnson (1983b) in the derivation of the Green function. However, as stated by Feng

and Johnson (1983a), if the dispersion equation with $\mathrm{Re}(k\xi_j) < 0$ has a complex velocity solution close to the real axis, its effect can be seen in the Green function. Therefore, Feng and Johnson (1983a) alternatively adopted the restriction $\mathrm{Re}(k\xi_j) - \mathrm{Im}(k\xi_j) \geq 0$, and found another pseudo-Rayleigh mode at very high frequencies that propagates faster than the fluid bulk mode but slower than the SV wave, which is in agreement with the results of the Green function. This restriction is analogous to the treatment of the pseudo-Rayleigh mode for the fluid/elastic solid case (Carcione and Helle 2004; Carcione et al. 2018).

When the restriction $\mathrm{Re}(k\xi_j) - \mathrm{Im}(k\xi_j) \geq 0$ is applied, in addition to the pseudo-Stoneley and true Stoneley waves in Figs. 8, 9 and 10, our computation also predicts a pseudo-Rayleigh mode, in agreement with the results of Feng and Johnson (1983a). The corresponding phase velocity and dissipation factor as a function of frequency are displayed in Figs. 12 and 13. Unlike the R1 wave and pseudo-Stoneley wave in Figs. 5 and 9, the pseudo-Rayleigh mode in this case suffers a very significant attenuation for all frequencies, indicating that its propagation is restricted. The results are similar to those observed by Feng and Johnson (1983a) and Chao et al. (2006). The reason is because the pseudo-Rayleigh mode at a fluid/porous medium interface radiates energy into the slow wave and the fluid bulk mode, and is damped by a combination of radiation and viscous fluid-solid interaction, as was investigated in Gubaidullin et al. (2004).

The effect of mesoscopic flow is similarly observed at low frequencies, causing velocity dispersion and attenuation between 10 and 300 Hz. The phase velocities with open BC decrease at high frequencies, whereas those with sealed BC increase, a phenomenon quite

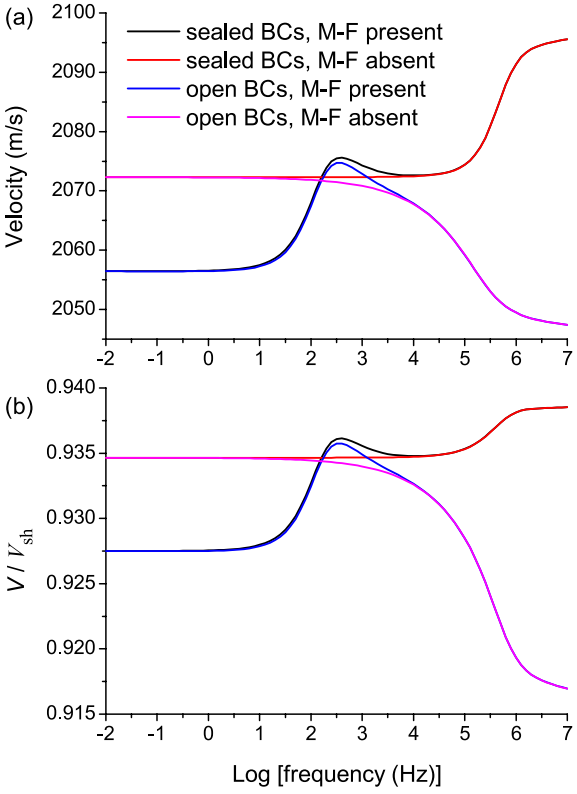

Fig. 12 Phase velocity (**a**) and phase dimensionless velocity with respect to V_{sh} (**b**) of the pseudo-Rayleigh waves as a function of frequency, at the interface between water and a porous half-space

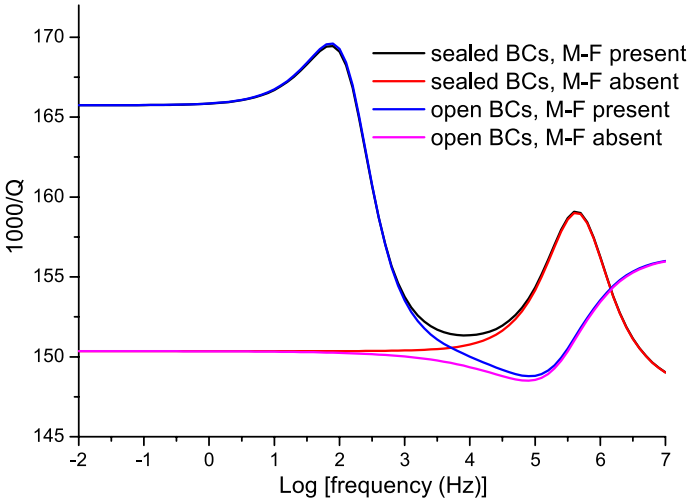

Fig. 13 Dissipation factor of the pseudo-Rayleigh wave as a function of frequency, at the interface between water and a porous half-space

different from the pseudo-Stoneley case, which is similarly observed in Gubaidullin et al. (2004) for open BC. It should be noted that the pseudo-Rayleigh mode propagates under certain conditions depending on the stiffness of both the porous solid and fluid. For example, if the shear-wave velocity is smaller than the bulk fluid velocity, there is no pseudo-Rayleigh mode (Feng and Johnson 1983a).

5.3 Waves at the Interface Between a Water Layer and a Porous Medium

Finally, we consider the general case with a finite thickness H of the water layer. Such case can be relevant for studying surface-wave propagations at the ocean floor, with seabed modeled as a heterogeneous porous medium and overlaid by a layer of seawater. In addition to the true Stoneley wave, the calculations predict high-order surface modes, as displayed in Fig. 14, quite similar to the results of elastic layered media. The cut-off frequency regards the higher-order modes, and it increases with increasing order. (The number of modes increases at high frequency.) Decreasing H implies an increased cut-off frequency for each mode. At the cut-off frequency, the velocity of each mode has an upper limit equal to the shear-wave velocity, and it decreases with increasing frequency, reaching a limit at high frequencies equal to 1490 m/s, the velocity of the acoustic wave in water, indicating that the higher-order modes are pseudo-Rayleigh waves.

Figure 15 shows the phase velocity and dissipation factor of the fundamental mode for four different values of H. At the low-frequency limit, the velocity tends to an asymptotic value of 1991 m/s = 0.898 V_{sh}, corresponding to the velocity of the pseudo-Rayleigh wave (R1) traveling along the free surface of a porous half-space (see Fig. 4). At high frequencies, the velocity becomes identical to that of $H = +\infty$, corresponding to the propagation of a pseudo-Stoneley wave (see Fig. 8). As a consequence, there is stronger velocity dispersion and attenuation at intermediate frequencies between 1 Hz and 1 kHz, unlike the case $H = +\infty$. The larger the H the weaker the attenuation, and the lower the dispersion frequency. Note that the velocity at low frequencies is higher

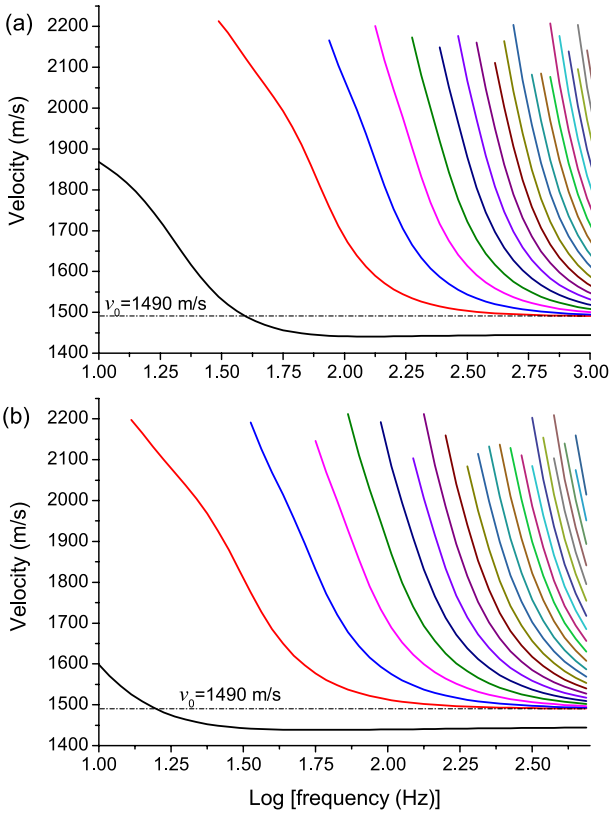

Fig. 14 Phase velocity of the surface waves as a function of frequency at the interface between a finite water layer and a porous half-space, with thickness **a** $H = 20$ m and **b** $H = 50$ m. The BC are sealed and the mesoscopic flow is assumed present. The black lines represent the results of the fundamental mode, whereas the coloured lines indicate the results of high-order surface modes. The dashed line represents the fluid bulk velocity v_0. The surface mode having velocity higher than v_0 is the pseudo-Rayleigh wave, whereas that with velocity smaller than v_0 is the pseudo-Stoneley wave

than the bulk fluid velocity v_0, but at high frequencies, it becomes lower. This implies that the fundamental mode is the pseudo-Rayleigh wave at low frequencies but it becomes the pseudo-Stoneley wave at high frequencies. The effect of the BC is noticed at high frequencies, since at low frequencies, the slow wave does not propagate. The open BC predict a higher attenuation and consequently a slightly higher velocity dispersion, than those of the sealed-pore case, which is not dependent on H.

Figure 16 shows the absolute displacements of the fundamental mode (pseudo-Stoneley wave) as a function of depth at 100 Hz with $H = 20$ m and $H = 50$ m. The behavior is quite similar as in Fig. 11. The energy does not completely decay at the water surface when $H = 20$ m, unlike the case $H = 50$ m. The mesoscopic-flow attenuation slightly affects the displacements, and the effect is more significant in the water layer. Figure 17 shows the displacements of the fundamental mode for $H = 5$ m (pseudo-Rayleigh wave), corresponding to 0.31 times the pseudo-Rayleigh wavelength. The vertical displacements are continuous at the interface whereas the horizontal ones are not. The horizontal displacement in water is higher and significantly decays to zero at the water surface. The critical depth in the porous medium is 16 m, approximately the pseudo-Rayleigh wavelength.

Figure 18 shows the phase velocity and dissipation factor of the first-order surface mode for $H = 20$ m and 50 m, when sealed-pore BC are used. The mesoscopic flow induces an evident attenuation peak, and results in a slight decrease of the phase

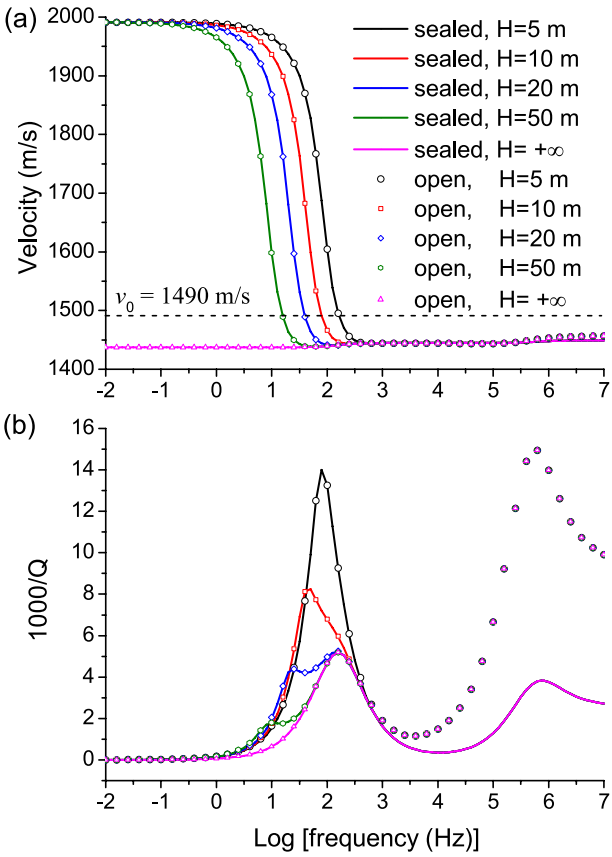

Fig. 15 Phase velocity (**a**) and dissipation factor (**b**) of the fundamental mode as a function of frequency at the interface between a water layer and a porous half-space for four different values of thickness H, when the mesoscopic-flow is present. The results of $H = +\infty$ are displayed for comparison. The dashed line in (**a**) corresponds to the velocity of the fluid bulk velocity $v_0 = 1490$ m/s. The mode is the pseudo-Rayleigh wave at low frequencies since the velocity is larger than v_0, whereas it is the pseudo-Stoneley wave at high frequencies where the velocity is smaller than v_0

velocity. The larger thickness H implies a smaller relaxation frequency. The behavior is similar for the other high-order modes.

In addition to the high-order surface modes, the computation with sealed-pore BC also gives the true Stoneley wave, as displayed in Fig. 19. We observe that this wave resembles the bulk slow P2 wave, except for a slight difference at high frequencies. Its propagation is not evidently affected by the thickness H, and the results overlap that of $H = +\infty$.

6 Discussions

The present study presents a theoretical analysis for surface-wave dispersion due to mesoscopic flow. Evidence from laboratory measurements and field observations is still lacking, possibly because of the difficulty in conducting the measurements, and because the observed data may also be affected by scattering attenuation in the presence of strong heterogeneities. Adler and Nagy (1994) measured the ultrasonic velocity dispersion and attenuation of the surface waves at the water/porous medium interface. Their results are consistent with the theoretical predictions of Feng and Johnson (1983a). In particular, their results demonstrate the existence of the slow true surface (Stoneley) wave when the BC is sealed. They attributed the attenuation to the viscous drag between the saturating fluid and

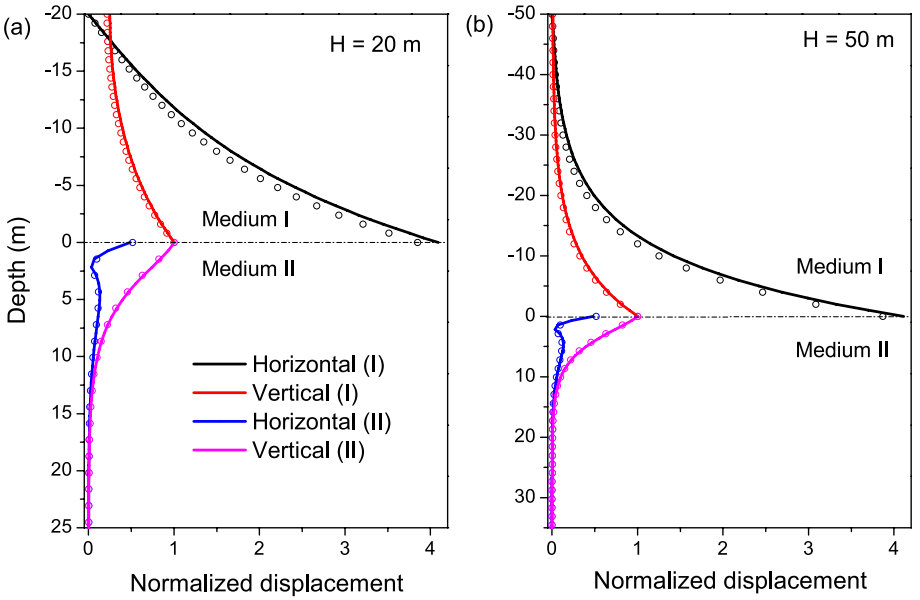

Fig. 16 Absolute values of the displacements of the fundamental mode (the pseudo-Stoneley wave) as a function of depth at 100 Hz, for two different values of H. The displacements are normalized by the vertical u_z at the surface $z = 0$ when the mesoscopic-flow is present. The open-pore BC are used. The solid and dotted lines represent the results without and with mesoscopic-flow attenuation, respectively

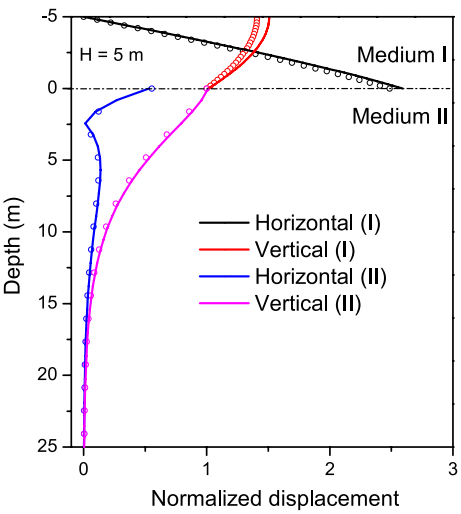

Fig. 17 Absolute values of the displacement of the fundamental mode (the pseudo-Rayleigh wave) as a function of depth at 100 Hz, for $H = 5$ m. The displacements are normalized by the vertical u_z at the surface $z = 0$ when the mesoscopic flow is present. The sealed-pore BC are used. The solid and dotted lines represent the results without and with mesoscopic-flow attenuation, respectively

the porous frame. The mesoscopic flow is not mentioned, since the measurement is made at ultrasonic frequencies.

In this work, the dispersion equation is numerically solved by using the Muller iteration method. One way to verify the solutions is to derive the analytical Green function for the fluid/porous medium interface system. Feng and Johnson (1983b) derived the 2D reflection

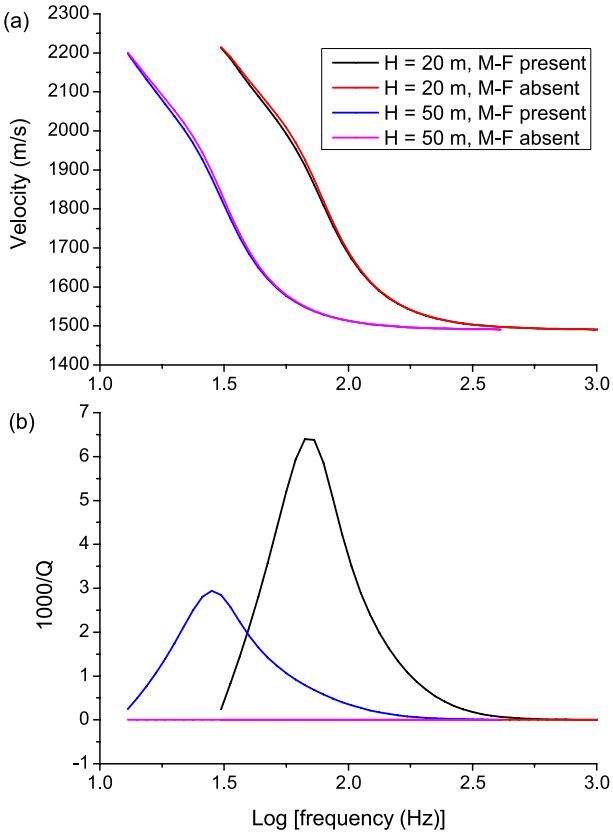

Fig. 18 Phase velocity (**a**) and dissipation factor (**b**) of the first-order surface mode (the pseudo-Rayleigh wave), at the interface between a water layer and a porous half-space with two different values of thickness H and sealed-pore BC

Green function based on the Cagniard-de Hoop method, but their results hold for the high-frequency limit of the classical Biot theory (Carcione 2022), where the viscous dissipation is ignored, which therefore cannot be directly applied here.

For layered porous media, not considered here, the results can be more complex. For example, at the free surface of layered porous media, there are higher-order Rayleigh modes, similar to the case of layered elastic solids. These modes are pseudo-Rayleigh waves because they leak energy into the slow P2 wave. Their signatures depend on the medium properties and frequency. Generally, the velocity of the fundamental mode ranges between the $V_r^{\max}$ at low frequencies and $V_r^{\min}$ at high frequencies, with $V_r^{\max}$ and $V_r^{\min}$ representing the maximum and minimum phase velocities of the pseudo-Rayleigh waves that propagate at the surface of each porous layer. Whereas the high-order modes have velocities ranging from the $V_s^{\max}$ at the cut-off frequencies and $V_s^{\min}$ at high frequencies, with $V_s^{\max}$ and $V_s^{\min}$ representing the maximum and minimum velocities of the shear waves among the layered media. For intermediate frequencies, both the fundamental and high-order modes undergo a velocity decrease, due to a geometrical dispersion mechanism present in layered media. On the contrary, the mesoscopic-flow mechanism increases the velocity at these frequencies, as shown in Fig. 4, a consequence of the velocity increase in the body waves. These are the two mechanisms affecting the surface-wave dispersion in layered media, which are generally coupled together, making the propagation more complex. In real cases,

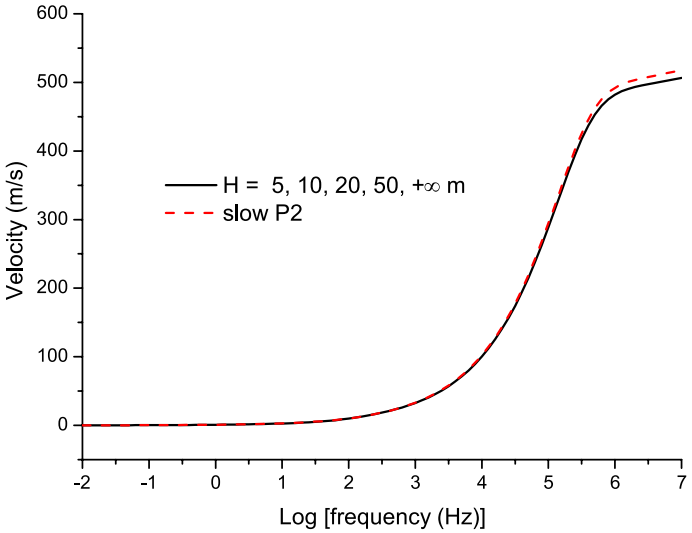

Fig. 19 Phase velocities of the true Stoneley wave at the interface between a water layer and a porous half-space with different values of thickness H and sealed-pore BC. The result of slow P2 wave is plotted (in dashed line) as a comparison. Note that the results with different H overlap. With the open-pore BC, the true Stoneley wave does not exist

the variations in shear-wave velocity in layered media are much more significant, and hence the geometrical dispersion plays a dominant role, causing decreased velocities from low to high frequencies. The detailed influence of the mesoscopic flow on surface-wave propagation in layered porous media will be investigated in a future study.

In real applications, it is a common practice to use the surface-wave velocity dispersion and attenuation to estimate the formation properties like the permeability and shear velocity (e.g., Cheng and Cheng 1996; Tang and Cheng 1996). Neglecting the attenuation induced by mesoscopic flow affects the interpretation. The results presented here can provide insights for improving quantitative reservoir characterization on the basis of surface-wave properties. Ongoing research includes the effect of the medium properties.

Shear-wave attenuation due to mesoscopic flow is not considered in the present work. This attenuation can be modeled by using a complex modulus based on the viscoelastic theory (e.g., Liu et al. 2018), or a fluid-flow based unrelaxed mechanism (e.g., Mavko and Jizba 1991), which will be investigated in a future work.

7 Conclusions

We have analyzed the propagation of surface waves at the interface separating a water layer and a porous medium described by the so-called effective Biot theory where mesoscopic-flow attenuation plays an important role. Special cases are considered by assuming the thickness of the water layer to be zero and infinity, corresponding to the propagation of Rayleigh- and Stoneley-type waves. In the case we study, we find a pseudo-Rayleigh wave and a true (Stoneley) mode at the surface of a porous half-space (zero thickness), whereas for infinite thickness, we predict a pseudo-Stoneley wave, a pseudo-Rayleigh wave, and a true surface mode. The mesoscopic flow mainly affects the propagation of pseudo waves at frequencies lower

than 10 kHz, particularly at the seismic band, inducing an attenuation peak and consequently velocity dispersion, whereas the effect of the boundary conditions (open and closed) is mainly observed at high frequencies. True Stoneley wave exists only for sealed boundary conditions and resembles the slow P2 wave, which is hardly affected by the mesoscopic flow. In the case of a nonzero thickness of the water layer, in addition to the true Stoneley wave, we predict high-order surface modes. The mesoscopic flow similarly induces an extra attenuation peak for each mode, which decreases and moves to lower frequencies as the thickness increases.

Appendix A: Complex Coefficients of the Effective Biot Medium

From Pride et al. (2004) and Liu et al. (2009), the complex coefficients are

$$\begin{aligned} a_{11}^{*} =& a_{11} - \frac{\mathrm{i}\omega a_{13}^2}{\mathrm{i}\omega a_{33} - \gamma(\omega)}, \quad a_{12}^{*} = a_{12} - a_{13}\frac{\mathrm{i}\omega a_{23} + \gamma(\omega)}{\mathrm{i}\omega a_{33} - \gamma(\omega)}, \\ a_{22}^{*} =& a_{22} + a_{23} - (a_{23} + a_{33})\frac{\mathrm{i}\omega a_{23} + \gamma(\omega)}{\mathrm{i}\omega a_{33} - \gamma(\omega)}, \end{aligned} \tag{A1}$$

where a_{ij} are the real double-porosity constants corresponding to the high-frequency response for which no internal fluid pressure relaxation can take place. These real coefficients are (Pride et al. 2004)

$$\begin{aligned} a_{11} =& 1/K^d, \qquad a_{22} = \frac{v_1\alpha_1}{K_1^d}\left(\frac{1}{B_1} - \frac{\alpha_1(1-Q_1)}{1 - K_1^d/K_2^d}\right), \\ a_{12} =& -\frac{v_1 Q_1}{K_1^d}\alpha_1, \quad a_{23} = -\frac{\alpha_1\alpha_2 K_1^d/K_2^d}{(1 - K_1^d/K_2^d)^2}\left(\frac{1}{K^d} - \frac{v_1}{K_1^d} - \frac{v_2}{K_2^d}\right), \\ a_{13} =& -\frac{v_2 Q_2}{K_2^d}\alpha_2, \quad a_{33} = \frac{v_2\alpha_2}{K_2^d}\left(\frac{1}{B_2} - \frac{\alpha_2(1-Q_2)}{1 - K_2^d/K_1^d}\right), \end{aligned} \tag{A2}$$

where subscript $i = 1$ or 2 denotes the phase 1 or 2, respectively, v_i is the volume fraction, K_i^d is the bulk modulus of the dry-rock frame, K_d is the dry-rock bulk modulus of the composite,

$$Q_1 = \frac{1}{v_1}\frac{1 - K_2^d/K_\mathrm{d}}{1 - K_2^d/K_1^d}, \quad Q_2 = \frac{1}{v_2}\frac{1 - K_1^d/K_\mathrm{d}}{1 - K_1^d/K_2^d}, \tag{A3}$$

B_i is the Skempton coefficient,

$$B_i = \frac{K_\mathrm{s} - K_i^d}{K_\mathrm{s} - K_i^d + \phi_i K_i^d(K_\mathrm{s}/K_\mathrm{f} - 1)}, \tag{A4}$$

where K_s and K_f are the bulk moduli of the grains and fluid, respectively, and ϕ_i is the porosity. Moreover, α_i is the Biot-Willis coefficient of phase i, given by

$$\alpha_i = (1 - K_i^d/K_i^u)/B_i, \tag{A5}$$

where K_i^u is the Gassmann wet-rock bulk modulus (confining pressure change divided by dilatation for a sealed sample), and is given by

$$K_i^u = \frac{K_i^d}{1 - B_i(1 - K_i^d/K_s)}. \tag{A6}$$

Substituting equation (A6) into (A5), we obtain

$$\alpha_i = 1 - \frac{K_i^d}{K_s}. \tag{A7}$$

The frequency-dependent internal transport coefficient $\gamma(\omega)$ is derived by Pride et al. (2004) as

$$\gamma(\omega) = \gamma_m \sqrt{1 - i\frac{\omega}{\omega_m}}, \tag{A8}$$

where γ_m and ω_m are parameters dependent on the constituent properties and the mesoscopic geometry. When the embedded phase 2 is very permeable, γ_m can be expressed by

$$\gamma_m = -\frac{\kappa_1 K_1^d}{\eta L_1^2}\left[\frac{a_{12} + B_0(a_{22} + a_{33})}{R_1 - B_0/B_1}\right]\left[(1 + O(\kappa_1/\kappa_2)\right], \tag{A9}$$

where η is the fluid viscosity, κ_i is the permeability of phase i, B_0 is the static Skempton coefficient of the composite, given by

$$B_0 = -\frac{a_{12} + a_{13}}{a_{22} + 2a_{23} + a_{33}}, \tag{A10}$$

R_1 is the ratio of the average confining pressure in phase 1 to the pressure applied to the external surface of the double-porosity composite, given by

$$R_1 = Q_1 + \frac{\alpha_1(1 - Q_1)B_0}{1 - K_1^d/K_2^d} - \frac{v_2}{v_1}\frac{\alpha_2(1 - Q_2)B_0}{1 - K_2^d/K_1^d}, \tag{A11}$$

and L_1 represents the characteristic length of the fluid pressure gradient.

In terms of γ_m, ω_m is

$$\omega_m = \frac{\eta B_1 K_1^d}{\kappa_1 \alpha_1}\left(\gamma_m \frac{V}{S}\right)^2\left(1 + \sqrt{\frac{\kappa_1 B_2 K_2^d \alpha_1}{\kappa_2 B_1 K_1^d \alpha_2}}\right)^2, \tag{A12}$$

with V/S representing the volume-to-surface ratio, where S is the surface area of the interface between the two phases in each volume V of composite.

In a concentric sphere geometry (a composite (phase 1) of radius R contains a small sphere of radius a of phase 2), satisfying $\kappa_1/\kappa_2 \ll 1$,

$$L_1^2 = \frac{9}{14}R^2\left[1 - \frac{7}{6}\frac{a}{R} + O(a^3/R^3)\right], \quad \frac{V}{S} = \frac{R^3}{3a^2}. \tag{A13}$$

In this case, the volume fractions v_1 and v_2 are defined as

$$v_2 = \left(\frac{a}{R}\right)^3, \quad v_1 = 1 - v_2, \tag{A14}$$

and the total porosity is

$$\phi = v_1\phi_1 + v_2\phi_2. \tag{A15}$$

Appendix B: Components of Matrix M

The elements of matrix **M** are

$$M_{00} = 0, \;\; M_{01} = 2\xi_1, \;\; M_{02} = 2\xi_2, \;\; M_{03} = -\mathrm{i}(1 + \xi_3^2), \tag{B1}$$

$$\begin{aligned} M_{10} &= -(1 - \exp[-2kH\xi_0])\rho_0, \\ M_{11} &= (A + Q + v_1(R + Q) + 2N)(1/V_1^2) - 2N/c^2, \\ M_{12} &= (A + Q + v_2(R + Q) + 2N)(1/V_2^2) - 2N/c^2, \\ M_{13} &= 2\mathrm{i}N\xi_3/c^2, \end{aligned} \tag{B2}$$

$$\begin{aligned} M_{20} &= \xi_0(1 + \exp[-2kH\xi_0]), \\ M_{21} &= \xi_1(1 - \phi + \phi v_1), \\ M_{22} &= \xi_2(1 - \phi + \phi v_2), \\ M_{23} &= -\mathrm{i}(1 - \phi + \phi v_3), \end{aligned} \tag{B3}$$

$$\begin{aligned} M_{30} &= -(1 - \exp[-2kH\xi_0])\rho_0, \\ M_{31} &= (Q + Rv_1)/\phi/V_1^2 + \mathrm{i}(v_1 - 1)\frac{\xi_1}{c}Z_I\phi, \\ M_{32} &= (Q + Rv_2)/\phi/V_2^2 + \mathrm{i}(v_2 - 1)\frac{\xi_2}{c}Z_I\phi, \\ M_{33} &= (v_3 - 1)\frac{1}{c}Z_I\phi. \end{aligned} \tag{B4}$$

Next, we compare the above equations with those of Feng and Johnson (1983a). By letting $H = +\infty$ and $P = A + 2N$, and defining

$$\begin{aligned} D_0 &= C_0, \;\; D_1 = C_1, \;\; D_2 = C_2, \;\; D_3 = iC_3, \\ v_1 &= -G_+, \;\; v_2 = -G_-, \;\; v_3 = \frac{\tilde{\tau} - 1}{\tilde{\tau}}, \;\; Z_I = T, \end{aligned} \tag{B5}$$

in the same manner as Feng and Johnson (1983a), the first equation in (30) becomes

$$2\xi_1 C_1 + 2\xi_2 C_2 + (1 + \xi_3^2)C_3 = 0. \tag{B6}$$

By substituting ξ_j in equation (25) into (B6), we derive equation (C2) of Feng and Johnson (1983a).

The second equation in (30) becomes

$$\rho_0 c^2 C_0 + \left(\frac{\left[G_+(R+Q) - (P+Q) \right] c^2}{V_1^2} + 2N \right) C_1 + \left(\frac{\left[G_-(R+Q) - (P+Q) \right] c^2}{V_2^2} + 2N \right) C_2 + 2N\xi_3 C_3 = 0, \tag{B7}$$

which is Eq. (C1) of Feng and Johnson (1983a).

The third equation in (30) becomes

$$\xi_0 C_0 + \xi_1 (1 - \phi - \phi G_+) C_1 + \xi_2 (1 - \phi - \phi G_-) C_2 + \left(1 - \frac{\phi}{\tilde{\tau}} \right) C_3 = 0, \tag{B8}$$

which is equation (C3) of Feng and Johnson (1983a), where they instead use $\alpha = \tau$.

The last equation in (30) becomes

$$-\rho_0 C_0 + \left[\frac{Q - RG_+}{\phi V_1^2} - \mathrm{i} \frac{(G_+ + 1)\xi_1 T\phi}{c} \right] C_1 + \left[\frac{Q - RG_-}{\phi V_2^2} - \mathrm{i} \frac{(G_- + 1)\xi_2 T\phi}{c} \right] C_2 - \mathrm{i} \frac{T\phi}{c\tilde{\tau}} C_3 = 0. \tag{B9}$$

By multiplying $-\phi c^2$ on both sides, we derive equation (C4) of Feng and Johnson (1983a).

It is evident that the equations of Feng and Johnson (1983a) are special cases of our equations when $H = +\infty$. Moreover, our equations use frequency-dependent elastic coefficients associated with the mesoscopic fluid flow, and hence are more realistic for low-frequency surface-wave propagation.

Acknowledgements We appreciate the comments from the Editor Michael J. Rycroft and three anonymous reviewers, which significantly improve this manuscript. This work has been supported by the "National Nature Science Foundation of China (42174148, 41804095)," the "China Postdoctoral Science Foundation (2020M682242)," and the Qingdao Postdoctoral Applied Research Project.

Data Availability Data and codes can be available by contacting the corresponding author.

Declarations

Conflict of Interest The authors declare that they have no conflict of interest.

References

Adler L, Nagy PB (1994) Measurements of acoustic surface waves on fluid-filled porous rocks. J Geophys Res Solid Earth 99(B9):17863–17869

Ba J, Carcione JM, Nie J (2011) Biot–Rayleigh theory of wave propagation in double-porosity media. J Geophys Res Solid Earth 116:B06202

Berryman JG, Wang HF (2000) Elastic wave propagation and attenuation in a double-porosity dual-permeability medium. Int J Rock Mech Min Sci 37(1–2):63–78

Biot MA (1956) Theory of propagation of elastic waves in a fluid-saturated porous solid. I. Low frequency range. J Acoust Soc Am 28(2):168–178

Biot MA (1962) Mechanics of deformation and acoustic propagation in porous media. J Appl Phys 33(4):1482–1498

Carcione JM (2022) Wave Fields in Real Media. Theory and numerical simulation of wave propagation in anisotropic, anelastic, porous and electromagnetic media. Elsevier Amsterdam (Fourth edition, extended and revised)
Carcione JM, Gurevich B (2011) Differential form and numerical implementation of Biot's poroelasticity equations with squirt dissipation. Geophysics 76(6):N55–N64
Carcione JM, Helle HB (2004) The physics and simulation of wave propagation at the ocean bottom. Geophysics 69(3):825–839
Carcione JM, Morency C, Santos JE (2010) Computational poroelasticity—a review. Geophysics 75:A229–A243
Carcione JM, Bagaini C, Ba J, Wang E, Vesnaver A (2018) Waves at fluid-solid interfaces: explicit versus implicit formulation of the boundary condition. Geophys J Int 215(1):37–48
Carcione JM, Gei D, Gurevich B, Ba J (2021) On the normal-incidence reflection coefficient in porous media. Surv Geophys 42(4):923–942
Chao G, Smeulders DMJ, Van Dongen MEH (2006) Dispersive surface waves along partially saturated porous media. J Acoust Soc Am 119(3):1347–1355
Cheng N, Cheng CH (1996) Estimations of formation velocity, permeability, and shear-wave anisotropy using acoustic logs. Geophysics 61(2):437–443
Dahl EJ, Spikes KT (2017) Local and global fluid effects on sonic wave modes. Geophysics 82(6):D369–D381
Dai ZJ, Kuang ZB, Zhao SX (2006) Rayleigh waves in a double porosity half-space. J Sound Vib 298(1–2):319–332
Deresiewicz H (1962) The effect of boundaries on wave propagation in a liquid-filled porous solid: IV. Surface waves in a half-space. Bull Seismol Soc Am 52(3):627–638
Deresiewicz H (1964) The effect of boundaries on wave propagation in a liquid-filled porous solid: VII. Surface waves in a half-space in the presence of a liquid layer. Bull Seismol Soc Am 54(1):425–430
Deresiewicz H, Skalak R (1963) On uniqueness in dynamic poroelasticity. Bull Seismol Soc Am 53(4):783–788
Dvorkin J, Nur A (1993) Dynamic poroelasticity: a unified model with the squirt and the Biot mechanisms. Geophysics 58(4):524–533
Dvorkin J, Mavko G, Nur A (1995) Squirt flow in fully saturated rocks. Geophysics 60(1):97–107
Feng S, Johnson DL (1983a) High-frequency acoustic properties of a fluid/porous solid interface. I. New surface mode. J Acoust Soc Am 74(3):906–914
Feng S, Johnson DL (1983b) High-frequency acoustic properties of a fluid/porous solid interface. II. The 2D reflection Green's function. J Acoust Soc Am 74(3):915–924
Gubaidullin AA, Kuchugurina OY, Smeulders DMJ, Wisse CJ (2004) Frequency-dependent acoustic properties of a fluid/porous solid interface. J Acoust Soc Am 116(3):1474–1480
Gurevich B, Ciz R, Denneman AI (2004) Simple expressions for normal-incidence reflection coefficients from an interface between fluid-saturated porous materials. Geophysics 69(6):1372–1377
Han Q, Qi L, Shan M, Yin C, Jiang X, Zhu C (2017) Propagation characteristics of interface waves between a porous medium and a sediment-containing two-phase fluid. Ultrasonics 81:73–80
Johnson DL, Koplik J, Dashen R (1987) Theory of dynamic permeability and tortuosity in fluid-saturated porous media. J Fluid Mech 176:379–402
Liu X, Greenhalgh S, Zhou B (2009) Transient solution for poro-viscoacoustic wave propagation in double porosity media and its limitations. Geophys J Int 178(1):375–393
Liu X, Greenhalgh S, Zhou B, Heinson G (2016) Generalized poroviscoelastic model based on effective Biot theory and its application to borehole guided wave analysis. Geophys J Int 207(3):1472–1483
Liu X, Greenhalgh S, Zhou B, Greenhalgh M (2018) Effective Biot theory and its generalization to poroviscoelastic models. Geophys J Int 212(2):1255–1273
Lo WC (2008) Propagation and attenuation of Rayleigh waves in a semi-infinite unsaturated poroelastic medium. Adv Water Resour 31(10):1399–1410
Lo WC, Sposito G, Majer E (2005) Wave propagation through elastic porous media containing two immiscible fluids. Water Resour Res 41(2):W02025
Markov MG (2009) Low-frequency Stoneley wave propagation at the interface of two porous half-spaces. Geophys J Int 177(2):603–608
Masson YJ, Pride SR (2007) Poroelastic finite difference modeling of seismic attenuation and dispersion due to mesoscopic-scale heterogeneity. J Geophys Res: Solid Earth 112(B3):3204
Masson YJ, Pride SR (2011) Seismic attenuation due to patchy saturation. J Geophys Res: Solid Earth 116(B3). https://doi.org/10.1029/2010JB007983
Mavko G, Jizba D (1991) Estimating grain-scale fluid effects on velocity dispersion in rocks. Geophysics 56(12):1940–1949
Mayes MJ, Nagy PB, Adler L, Bonner BP, Streit R (1986) Excitation of surface waves of different modes at fluid-porous solid interface. J Acoust Soc Am 79(2):249–252
Muller DE (1956) A method for solving algebraic equations using an automatic computer. Math Tables Other Aids Comput 10(56):208–215

Müller TM, Gurevich B, Lebedev M (2010) Seismic wave attenuation and dispersion resulting from wave-induced flow in porous rocks-a review. Geophysics 75(5):75A147-75A164
Norris AN (1989) Stoneley-wave attenuation and dispersion in permeable formations. Geophysics 54(3):330–341
Pan Y, Gao L, Bohlen T (2019) High-resolution characterization of near-surface structures by surface-wave inversions: from dispersion curve to full waveform. Surv Geophys 40(2):167–195
Pride SR, Berryman JG (2003a) Linear dynamics of double porosity dual-permeability materials. I. Governing equations and acoustic attenuation. Phys Rev E 68(3):036603
Pride SR, Berryman JG (2003b) Linear dynamics of double porosity dual-permeability materials. II. Fluid transport equations. Phys Rev E 68(3):036604
Pride SR, Berryman JG, Harris JM (2004) Seismic attenuation due to wave-induced flow. J Geophys Res: Solid Earth 109(B1). https://doi.org/10.1029/2003JB002639
Qi Q, Cao J, Wang X, Gao J (2021) Influence of interface condition on reflection of elastic waves in fluid-saturated porous media. Geophysics 86(4):MR223–MR233
Qiu H, Xia T, Chen W, Yu B (2019) Low-frequency pseudo-Rayleigh and pseudo-Scholte waves at an interface of liquid/soft porous sediment with underlying hard porous sediment substrate. Geophys J Int 219(1):540–552
Sharma MD (2012) Rayleigh waves in a partially saturated poroelastic solid. Geophys J Int 189(2):1203–1214
Sharma MD (2014) Effect of local fluid flow on Rayleigh waves in a double porosity solid. Bull Seismol Soc Am 104(6):2633–2643
Sharma MD (2018) Squirt-flow in fluid-saturated porous media: propagation of Rayleigh waves. Transp Porous Media 122(1):25–42
Sidler R, Carcione JM, Holliger K (2010) Simulation of surface waves in porous media. Geophys J Int 183(2):820–832
Tajuddin M (1984) Rayleigh waves in a poroelastic half-space. J Acoust Soc Am 75(3):682–684
Tang X, Cheng CH (1996) Fast inversion of formation permeability from Stoneley wave logs using a simplified Biot–Rosenbaum model. Geophysics 61(3):639–645
Wang Y, Zhao L, Cao C, Yao Q, Yang Z, Cao H, Geng J (2022) Wave-induced fluid pressure diffusion and anelasticity in partially saturated rocks: the influences of boundary conditions. Geophysics 87(5):MR247–MR263
Xia J, Xu Y, Luo Y, Miller RD, Cakir R, Zeng C (2012) Advantages of using multichannel analysis of Love waves (MALW) to estimate near-surface shear-wave velocity. Surv Geophys 33(5):841–860
Zhang X, Müller TM (2019) Stoneley wave attenuation and dispersion and the dynamic permeability correction. Geophysics 84(4):WA1–WA10
Zhang Y, Xu Y, Xia J (2011) Analysis of dispersion and attenuation of surface waves in poroelastic media in the exploration-seismic frequency band. Geophys J Int 187(2):871–888
Zhang Y, Xu Y, Xia J, Ping P, Zhang S (2014) On dispersive propagation of surface waves in patchy saturated porous media. Wave Motion 51(8):1225–1236
Zhang L, Ba J, Carcione JM (2021) Wave propagation in infinituple-porosity media. J Geophys Res: Solid Earth 126(4):e2020JB021266
Zhang L, Ba J, Carcione JM, Wu C (2022) Seismic wave propagation in partially saturated rocks with a fractal distribution of fluid-patch size. J Geophys Res: Solid Earth 127(2):e2021JB023809
Zhao L, Han DH, Yao Q, Zhou R, Yan F (2015) Seismic reflection dispersion due to wave-induced fluid flow in heterogeneous reservoir rocks. Geophysics 80(3):D221–D235
Zhao L, Yuan H, Yang J, Han DH, Geng J, Zhou R, Li H, Yao Q (2017) Mobility effect on poroelastic seismic signatures in partially saturated rocks with applications in time-lapse monitoring of a heavy oil reservoir. J Geophys Res: Solid Earth 122(11):8872–8891
Zhao L, Wang Y, Yao Q, Geng J, Li H, Yuan H, Han DH (2021) Extended Gassmann equation with dynamic volumetric strain: modeling wave dispersion and attenuation of heterogeneous porous rocks. Geophysics 86(3):MR149–MR164